3-2021

Flow Banding Formation in Spherulitic Felsic to Intermediate Composition Dikes at Mt. Jasper, Berlin, New

Evelyn Randazzo

Flow Banding Formation in Spherulitic Felsic to Intermediate Composition Dikes at Mt. Jasper, Berlin, New

A Senior Thesis Presented to The
Faculty of the Department of Geology

Bates College

In partial fulfillment of the requirements for

the Degree of Bachelor of Arts

by
Evelyn Randazzo

Lewiston, Maine
December 15, 2020

Acknowledgements

I would like to thank my thesis advisor, Geneviève Robert, not only for the help and support that she has provided throughout my thesis writing journey, but also for her undying patience and devotion to teaching. In my time working with Geneviève as a student, TA and research assistant she has held high expectations and continued to facilitate my learning and equipped me with the knowledge and tools necessary to reach those goals.

I would also like to thank Dyk Eusden for helping advise my thesis, collecting my samples and for all of the guidance he has provided throughout my time at Bates. Dyk's enthusiasm for exploration and the outdoors is what initially drew me to geology and for that, I am forever grateful to him.

To all of the remaining faculty and staff members of the Bates geology department and to my fellow geology majors, thank you for your kindness, support and unmeasurable contributions to the wild ride we have all shared over the past four years.

A special thanks to Stephen Pollock, Richard Boisvert and Thomas Williams for taking an interest in my project and for sharing their previous work and knowledge of Mt. Jasper.

To my Mom, Dad and brothers, thank you for your never-ending love, support and encouragement.

Table of Contents

Table of Figures

Table of Tables

Abstract

This study presents structural and textural examinations as well as bulk chemical analyses for five felsic to intermediate composition dikes from Mt. Jasper, including one previously undiscovered rhyolite dike. The analyzed samples collectively display well to poorly pronounced flow banding, ranging from under 0.25 to 4 mm in thickness. The flow banding structures exhibit a range of morphologies including straight, curved, wavy, and nonuniformly thick banding as well as several instances of sheared flow banding. Multiple samples possess rounded, irregularly shaped spherules that are exclusively confined within the darker flow bands. Many of these spherules are enclosed by white or dark mineral rims. Chemical analyses deduced a range of SiO_2 contents from 54 to 84% and revealed variations in bulk chemistries observed in different areas of each of the individual samples.

Structural, textural and chemical observations indicate that the flow banding in the Mt. Jasper dikes is likely to have resulted from one or more of the following processes: 1) shear-induced fragmentation and reannealing of magma in the volcanic conduit, 2) shear-induced production of fracture networks and subsequent oxide microlite nucleation, 3) mingling of two compositionally distinct magmas, or 4) flow-induced stretching of magma containing zones of varying water concentrations. Further microtextural and chemical investigation is required to reach a more specific conclusion about which of these mechanisms is responsible for the flow banding in these dikes.

Chapter 1: Introduction

1.1 Project Overview

The study area which will be focused on in this project is Mt. Jasper, located in the city of Berlin, New Hampshire. The location of Mt. Jasper is indicated by the blue dot marked on the map of New Hampshire from the Billings and Fowler-Billings (1975) book provided in figure 1.1. There are several known felsic dikes located in and around Berlin. One of these dikes was recently discovered, in the summer of 2020, by John Dykstra Eusden and his undergraduate mapping team from Bates College. Many of these dikes exhibit weak to well defined flow banding that is oriented parallel to the walls of the dike intrusions. Flow banding structures observed within these dikes vary in morphology and in thickness, from approximately 0.05 to 5 mm (Billings and Fowler-Billings, 1975). This study will focus on ten felsic and intermediate composition rock samples collected from five dikes located at Mt. Jasper. One sample was sourced from the newly discovered dike near Mt. Jasper, one was collected at the railroad tracks in downtown Berlin, one from a quarry in Berlin, three from one dike at the Mt. Jasper archaeological site, and four from another dike at the Mt. Jasper archaeological site.

Flow banding is commonly found in silicic volcanic rocks (Gonnermann and Manga, 2004), however flow banded spherulitic rhyolites, like those found on Mt. Jasper are extremely uncommon in New England (Pollock et al., 2008). The study of flow banding structures is an integral part of understanding magma deformation associated with flow, as these structures record the deformational history of the magma from which they came. Information about the magma's ascent in the conduit, eruption and/or emplacement may be deduced from these preserved magmatic structures (Gonnermann and Manga, 2004). This area of study is particularly interesting in the context of the silicic dikes at Mt. Jasper, as no previous works have

attempted to investigate the specific magmatic mechanisms that produced the flow banding in these dikes.

1.2 Archaeological Significance of the Mt. Jasper Lithic Site

Since 1992, when the New Hampshire State Historic Review Board elected the Mt. Jasper Lithic Source to be included in the National Register of Historic Places, Mt. Jasper has been officially recognized as a famous archaeological site (Boisvert, 1992). This recognition is legitimized by the historical use of the site by Androscoggin Native Americans. Flow banded rhyolites sourced from dikes at Mt. Jasper were mined for approximately 8,500 years from the Early Archaic period to the Late Woodland period by these natives for the purpose of crafting sharp tools and projectiles from the rhyolite (Boisvert, 1992). The most heavily mined area, referred to as the Mt. Jasper mine, is located about 20 meters from the summit, on the steep southwestern exposure of the mountain, where an approximate 108 cubic meter cavity has been created in the rock (Boisvert, 1992). This major mine exists within the largest of Mt. Jasper's exposed rhyolite dikes, however several additional historical rhyolite mining sites are also present on the mountain (Boisvert, 1992). This flow banded rhyolite is very hard in nature and its glassy texture fractures to produce durable, blade-like edges, making it a very desirable material for tool manufacturing. Considering the volume of material that was mined from Mt. Jasper, it is likely that over a million artifacts were constructed from this rock (Boisvert, 1992).

1.3 Bedrock Geology

Mt. Jasper and the city of Berlin, New Hampshire are located within the northwestern corner of the Gorham 15' Quadrangle. The quadrangle encompasses 216 square miles of land

within New Hampshire and Maine, bounded by latitudes N.44˚15’ and N.44˚30’ and longitudes W.71˚00’ and W. 71˚15’ (Billings and Fowler-Billings, 1975). The location and area covered by the Gorham 15’ Quadrangle is enclosed by the red box on the map provided in figure 1.1. The quadrangle is comprised of five major stratigraphic units: 1) the Middle Ordovician age Ammonoosuc Volcanics, which are primarily composed of fine-grained gneiss and amphibolite (Oam), 2) the Middle Ordovician age biotite quartz monzonite (bqm) of the Oliverian Plutonic Series, 3) the Early Devonian-Late Silurian Littleton Formation, majorly comprised of paragneiss (Dlg), mica schist and feldspathic quartzite (Dlsg) in addition to minor areas of lime-silicate rocks (Dlb, Dll) and quartz conglomerates (Dlc), 4) the Middle Devonian age New Hampshire Plutonic Series, composed of diorite (dn), quartz diorite (qd), quartz monzonites (K, CO), and pegmatite (P), and 4) the Early Jurassic black diorite (dw) of the White Mountain Plutonic-Volcanic Series (Billings and Fowler-Billings, 1975). Each of these stratigraphic units are illustrated below in the bedrock geology map of the Gorham 15’ Quadrangle provided in figure 1.2 from Billings and Fowler-Billings (1975). The location of Mt. Jasper is indicated by a red dot on the map.

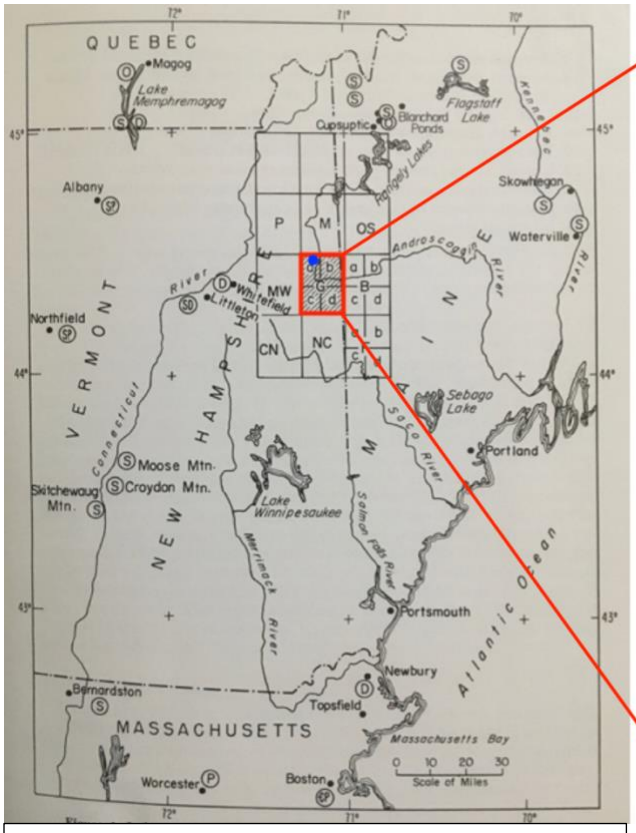

Figure 1.1: Location of the Gorham 15' Quadrangle (red box) and Mt. Jasper (blue dot) in central New Hampshire and Maine from Billings and Fowler-Billings (1975).

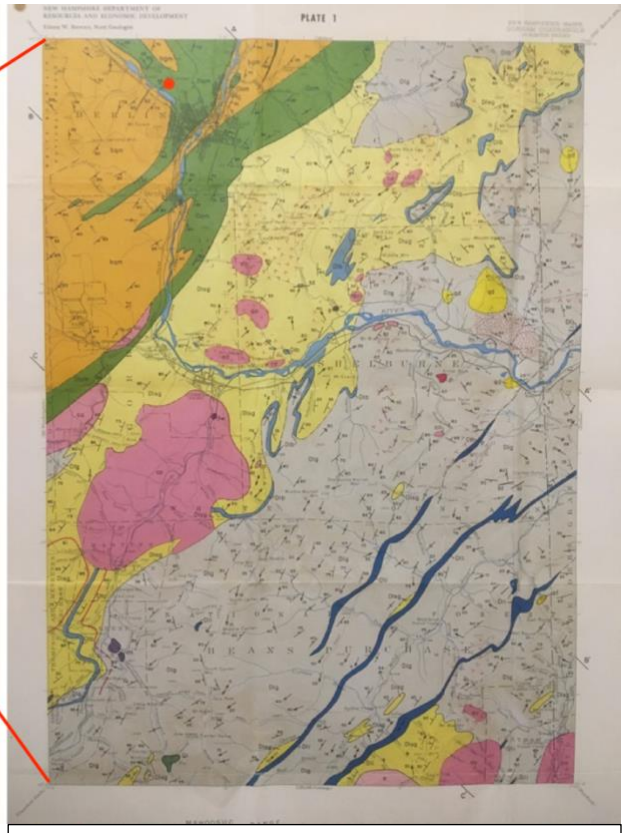

Figure 1.2: Gorham 15' Quadrangle bedrock geology map from plate 1 of the Billings and Fowler-Billings (1975) book. Red dot marks Mt. Jasper and green area represents the Ammonoosuc Volcanics region.

1.4 Gorham 15' Quadrangle Post-Metamorphic Dikes

Mt. Jasper lies within the Ammonoosuc Volcanics region of the quadrangle, which is confined to the green areas of the Billings and Fowler-Billings (1975) bedrock geology map in figure 1.2. Four varieties of dikes intruded the Ammonoosuc Volcanics at Mt. Jasper, including very coarse-grained to pegmatitic granitic dikes, a biotite granofels dike, basalt dikes, and the flow banded rhyolite dikes that will be focused on in this study (Billings and Fowler-Billings, 1975), (Pollock et al., 2008). 241 post-metamorphic dikes were mapped within the Gorham 15' Quadrangle in 1975 by Billings and Fowler-Billings. Thicknesses of these dikes range from several inches to 20 feet, with an average width of 3.5 feet (Billings and Fowler-Billings, 1975). The location and strikes of each of these dikes are plotted on the Gorham 15' Quadrangle map

provided in figure 1.3 from the Billings and Fowler-Billings (1975) book. A total of eight rhyolite dikes were mapped within this area, not including the newly discovered dike that will be introduced in this study. Each of these rhyolite dikes is highlighted in pink in the northwestern corner of the quadrangle map.

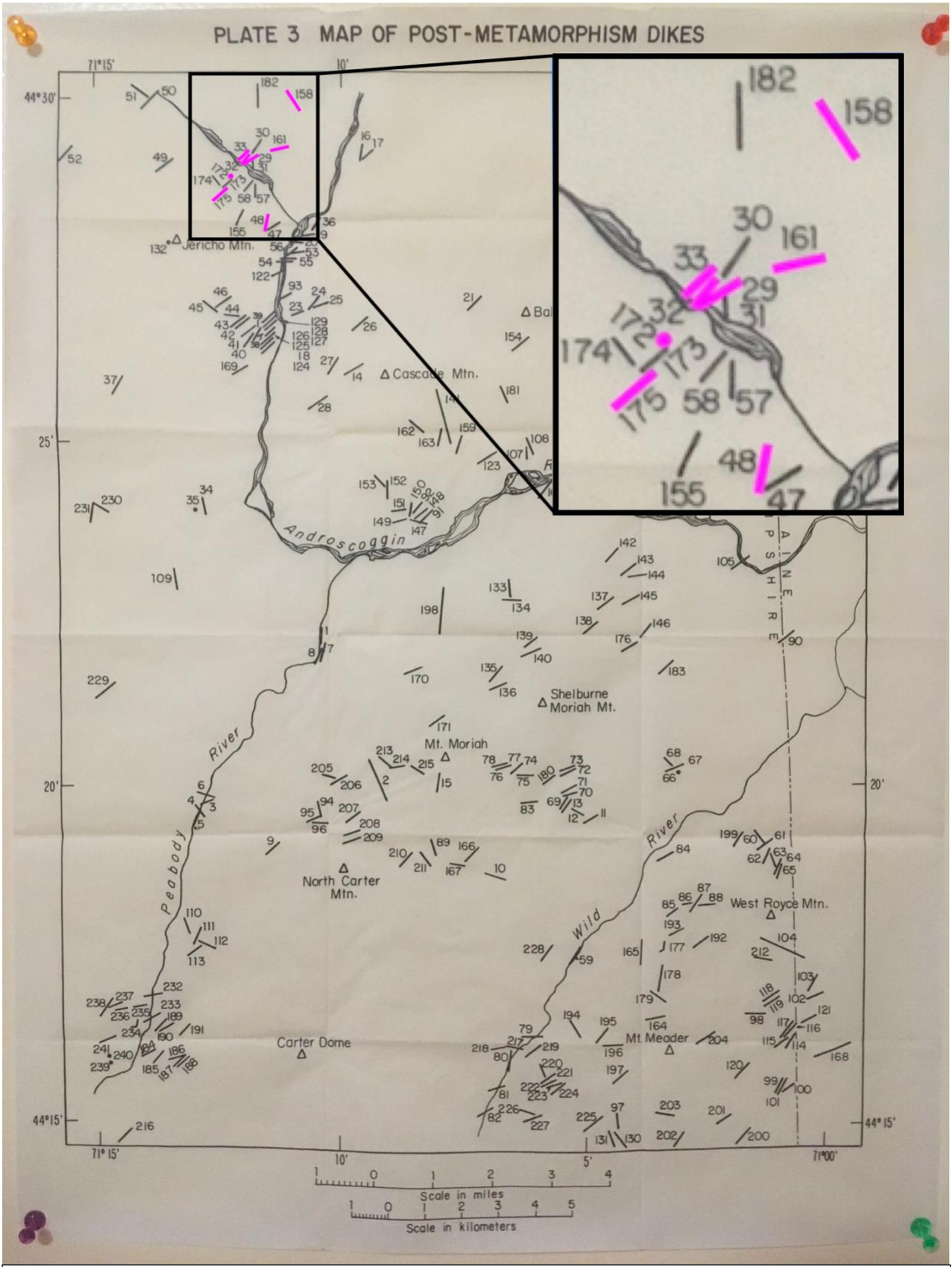

Figure 1.3: Plate 3 map of 241 post-metamorphic dikes within the Gorham 15' Quadrangle (Billings and Fowler-Billings, 1975). Rhyolite dikes (29, 32, 33, 48, 158, 161, 172 and 175) are highlighted in pink.

1.5 Tectonic Setting

Concentrated swarms of mafic dikes, like the majority of those found in this quadrangle, have been forming within the Appalachian region since the Late Precambrian (McHone et al., 1987). However, the post-metamorphic nature of the Gorham 15' Quadrangle dikes dates the dikes in this region to the Mesozoic (McHone et al., 1987). The age of these dikes can be further specified by their extensional stress regimes and corresponding tectonic events. Extensional stress regimes associated with large clusters of dikes, like those seen in the Gorham 15' Quadrangle, can be deduced by finding the average trend of the dikes and then locating the direction of extensional stress, which will be oriented perpendicularly to the average trend of the dikes (Faure et al., 2006). By this logic, the general NE-SW striking trends of the Gorham 15' Quadrangle dikes are indicative of a NW-SE paleostress regime.

NE-SW trending dikes and their relative NW-SE extensional regimes that exist within this particular northeastern region of North America are commonly associated with divergent plate motion between the North American and African plates (Faure et al., 2006). This divergence occurred with the rifting of Pangea and subsequent opening of the Northern Atlantic Ocean in the Late Triassic-Jurassic periods (Faure et al., 2006). Most geologic evidence of this particular tectonic event and paleostress environment exists in offshore sedimentation and faulting (Faure et al., 2006). The limited amount of evidence that can be seen on land is located in northeastern North America, where NE-SW trending dikes from this event and time period are common (Faure et al., 2006). Preservation of this SE-NW extensional regime recorded in one 158 million year old White Mountain Magma Series granite indicates that this Late Triassic-Jurassic extensional regime continued well into the Late Jurassic period (Faure et al., 2006).

Of the 241 dikes mapped by Billings and Fowler-Billings (1975), 233 possessed mafic

compositions including biotite granofels, basalt, diabase, porphyritic diabase, gabbro, diorite, and camptonite dikes (Billings and Fowler-Billings 1975, Pollock et al., 2008). The other eight dikes are those rhyolite dikes highlighted in pink in figure 1.3. These eight dikes are presumed to be associated with the White Mountain Plutonic Series (Pollock et al., 2008). A total of two bodies of rock belonging to the White Mountain Plutonic Series have been identified within the Gorham 15' Quadrangle. The first of these two is a diorite that is primarily composed of andesite, amphibole and biotite with minor amounts of magnetite, sphene, and carbonate (Billings and Fowler-Billings, 1975). The second body is a volcanic vent agglomerate comprised of clasts within a white crystalline matrix (Billings and Fowler-Billings, 1975). The clasts are primarily composed of a fine-grained porphyritic andesite with andesine-labradorite phenocrysts in a plagioclase, amphibole and biotite groundmass with minor amounts of magnetite (Billings and Fowler-Billings, 1975). The surrounding matrix is made up of granular quartz, feldspar and mica (Billings and Fowler-Billings, 1975). Billings and Fowler-Billings (1975) characterized these contrasting mafic and felsic compositional rocks of the Ammonoosuc Volcanics as being a part of a bimodal volcanic system, which is consistent with the continental rifting tectonic history associated with these dikes.

1.6 Flow Banding

Flow banding structures, like those seen in some of the Mt. Jasper dikes, are a form of igneous layering that can arise from either structural or mineralogical heterogeneity between the separate bands in the rock (Munro, 1990). Structural banding is characterized by visual differences in the structures, colors and textures within the bands (Munro, 1990). Although the magmatic mechanisms which cause structural flow banding are still relatively unknown, they

generally are a result of differing crystallinity, bubble content, or degree of development of spherulites (Munro, 1990). Mineralogical flow banding is a result of compositional variations between the band structures which can be produced by several different mechanisms (Munro, 1990).

One process that can result in mineralogical flow banding is the mixing of compositionally distinct magmas (Seaman et al., 1995, Gonnermann and Manga, 2004, Castro et al., 2005). In this instance, two parent magmas with varying chemistries mingle as they rise in one unifying volcanic conduit, resulting in the production of one hybrid magma with alternating regions or bands composed of chemically distinct material from each of the combined magma flows (Seaman et al., 1995, Gonnermann and Manga, 2004). Another possible mechanism for the formation of compositional banding is the crystallization of vapor-precipitated materials inside of bubbles within a magma (Gonnermann and Manga, 2004). This may happen when the formation of shear planes from laminar flow in the melt aligns the vesicles to create laterally continuous planes (Hausback, 1987).

Compositional flow banding may also form as a result of shearing of a compositionally heterogenous melt. This might occur by repeated autobrecciation followed by the reheating of partially cooled melt until it reaches its fully liquidus phase, otherwise known as reannealing, and subsequent deformation of the reannealed material (Gonnermann and Manga, 2004, Castro et al., 2005). This mechanism involves partial cooling and the application of shear stress on the basal zone of a lava flow (Smith, 1996). As the basal magma cools and begins to transition into a brittle phase, the shear stress applied by the overlying ductile flow ruptures and entrains fragments of the basal magma where it is reannealed within the flow of the overlying melt (Smith, 1996). An example of flow banding produced by this mechanism is shown in the

photograph from Smith (1996) provided in figure 1.4, where ductile shearing has produced multiple axial plane orientations with the repeated folding of the flow banding structures (Smith, 1996).

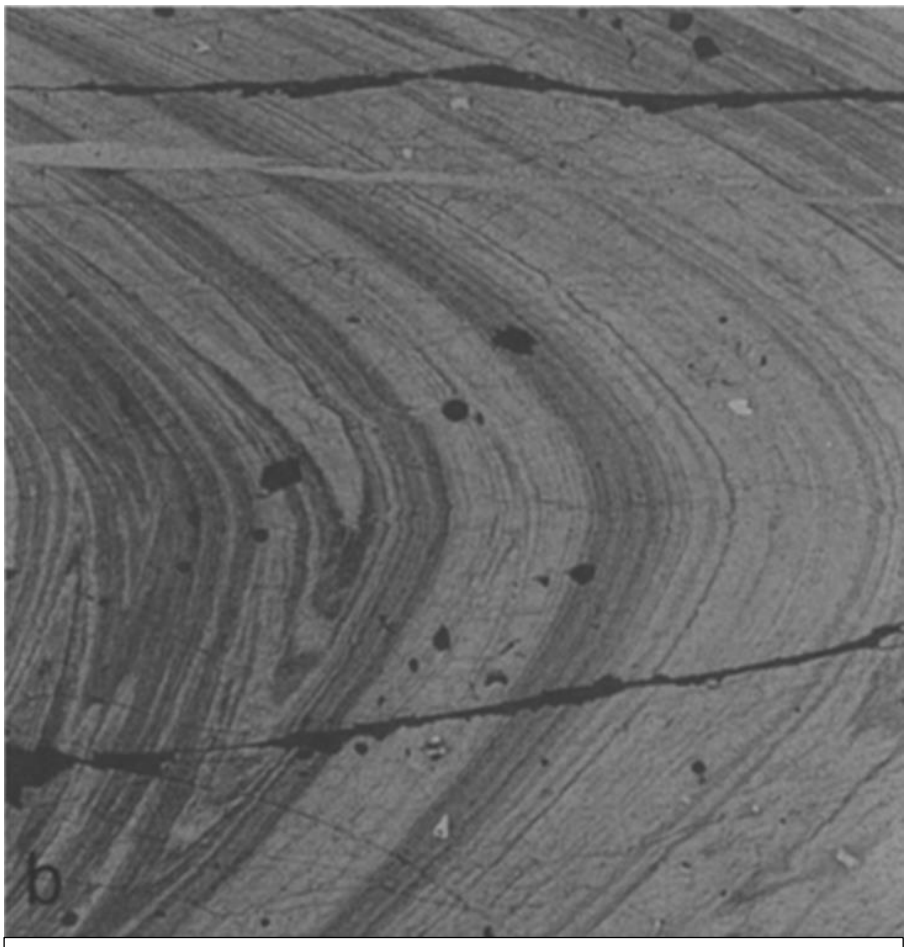

Figure 1.4: Repeated folding of flow banded lavas produced by autobrecciation, reannealing and deformation of basal material (Smith, 1996).

Welding and rheomorphism is another mechanism of flow banding formation that occurs with pyroclastic fragments (Gonnermann and Manga, 2004). Like autobrecciation and reannealing, this mechanism also deals with differential cooling rates throughout the volcanic conduit and brittle deformation, however it also involves fusion of fragmented material within the melt (Gottsmann and Dingwell, 2001). Another mechanism that is similar to autobrecciation and reannealing is the fragmentation and reannealing of magma along the conduit margins,

where microlite-rich magma at the conduit walls is fragmented by shear stress and reincorporated back into the flow (Gonnermann and Manga, 2003). In this instance, the flow banding formation occurs within the volcanic conduit rather than in the basal layer of the lava flow. In some cases, xenolithic material within the melt may be redistributed and aligned to form flow bands by similar mechanisms of shearing and deformation (Castro et al., 2005, Munro, 1990). These mechanisms are illustrated by the pyroclastic obsidian shown in figure 1.5 from the Rust et al. (2004) paper, where the flow banding was produced by the reannealing of brecciated, microlite-rich magma and by locally enriched bands of xenolithic fragments (Rust et al., 2004).

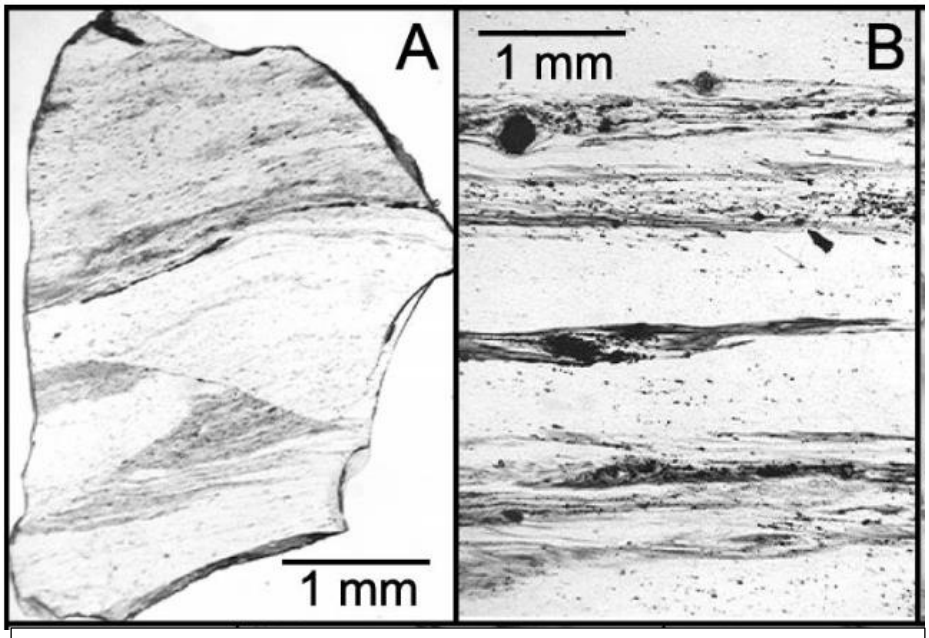

Figure 1.5: Flow banding in pyroclastic obsidian produced by alternating bands of differing microlite concentrations and alignment of dark colored xenolithic fragments (Rust et al., 2004).

1.7 Previous Works

Very few published works in geology have been dedicated exclusively to flow banding in the Mt. Jasper felsic dikes. The Gramly and Cox (1976) and Pollock et al. (2008) papers are among these few. Both of these papers discuss flow banded rhyolites from the Mt. Jasper lithic

source, however the specific locations of the sample collection sites are not specified. Pollock et al. (2008) presents a visual analysis of spherulitic flow banded rhyolites from Mt. Jasper and Mt. Jefferson. The authors suggest that the spherulitic textures found within Mt. Jasper's flow banded rhyolites are indicative of rapid undercooling, quenching and crystallization in the shallow intrusion (Pollock et al., 2008). The production of the flow banding was interpreted to be a result of laminar flow in the melt during the process of intrusion along with the development of a differential velocity profile where the movement of the melt was slower near the walls of the dike and faster at the center (Pollock et al., 2008). The numerical model developed in the Gonnermann and Manga (2003) study assumes that this type of velocity profile is typical for magma ascent in the volcanic conduit.

Gramly and Cox (1976) present a descriptive analysis of flow banding in the Mt. Jasper rhyolites. The rhyolites were described as cryptocrystalline, acidic igneous intrusives with very fine grained, glassy textures and distinct flow banding structures (Gramly and Cox, 1976). To the naked eye, the flow bands appear to have widths as great as 1 cm, however, when these bands were examined under a microscope, a series of many closely packed smaller bands were distinguished within the larger bands (Gramly and Cox, 1976). Centers of devitrification along the flow bands were observed under close examination in some samples (Gramly and Cox, 1976). In addition to the fresh specimen examination, descriptions of weathered surfaces indicated the presence of clouded, rusty weathering on the rocks (Gramly and Cox, 1976). Table 1.1 summarizes the results of a bulk chemical analysis of a Mt. Jasper rhyolite from Billings and Fowler-Billings (1975), which was reproduced in the Gramly and Cox (1976) paper. The results of this chemical analysis are consistent with Gramly and Cox's acidic rhyolite classification.

Oxide or Element	%	Oxide or Element	%
SiO_2	71.45	Na_2O	3.43
TiO_2	0.12	K_2O	6.67
Al_2O_3	13.35	H_2O-	0.00
Fe_2O_3	0.50	H_2O+	0.79
FeO	2.67	P_2O_5	trace
MnO	0.07	S	0.02_4
MgO	0.13	CO_2	0.03
CaO	0.52	BaO	0.03
			99.80_4

Table 1.1: Bulk chemical composition of a Mt. Jasper flow banded rhyolite sample (Billings and Fowler-Billings, 1975, Gramly and Cox, 1976).

1.8 Project Goals and Purposes

This study will present thorough structural and textural descriptions of three flow banded and two non-flow banded felsic to intermediate composition dikes at Mt. Jasper. In addition to these descriptive analyses, bulk chemistries of each sample will be collected and analyzed using the results gathered from XRF chemical analyses conducted for each specimen. The aim of this project will be to use all of these results to draw comparative observations in order to contextualize these five Mt. Jasper dikes within the broader scheme of the Gorham 15' quadrangle rhyolites and to ultimately identify the mechanisms of formation which resulted in flow banding in these Mt. Jasper dikes.

This study will expand our knowledge of the Mt. Jasper felsic dikes and introduce one newly discovered rhyolite dike that has not yet been mapped or documented in any previous works. The introduction of this new dike will open doors for geologists who have previously mapped and studied this area, because they will be allowed to consider this new feature in their

later studies as they build upon their previous work and acquire more complete and accurate future publications. The discovery may also present new research opportunities in the archaeological community, as further examination of this dike in the field could potentially lead to the detection of another unknown historical mining site. Archaeologists may also be able to compare the sample chemistries presented in this study with chemical compositions gathered from rhyolite artifacts of unknown origins to identify the exact dike from which the artifact was sourced.

Chapter 2: Methods

2.1 Instrument Details

All hand samples described in this study were collected by Dykstra Eusden, Liza Folsom, Tommy Sheils and Peter Galloway. The sample descriptions were completed by visually inspecting and studying the samples under a binocular microscope with a magnification range from 8x to 35x. Bulk chemical analyses were obtained using a portable X-Ray Fluorescence instrument (pXRF). The instrument used was an Olympus Vanta C-series VCR model pXRF with an Ag anode tube and an element range from Mg to U. The detection limit for this model is 3000 ppm. The Vanta C Series pXRF has a silicone drift detector which is protected by a Kapton mesh window. The excitation source is a 4-watt X-ray tube with a 40kV tube rating. An illustration of the pXRF from the Olympus Vanta C-series pXRF user manual is provided in figure 2.1.

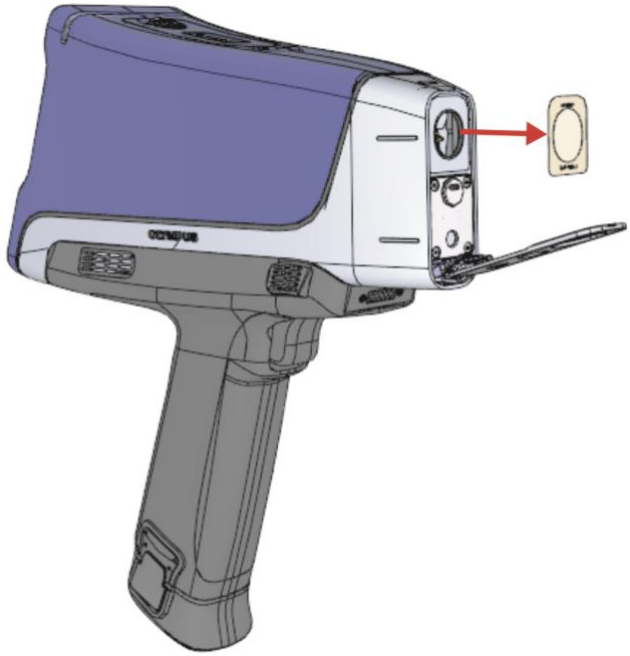

Figure 2.1: Olympus Vanta C-series pXRF (Olympus, 2020).

2.2 XRF Spectrometry

XRF spectrometry is a chemical analysis technique which determines the bulk elemental composition of a material by exciting atoms within the material with high energy external X-rays so that the atoms emit photons that can be used to identify and quantify the elements present in the material (Guthrie, 1996). This process begins by striking the sample with a high energy electron beam from the X-ray tube. The X-ray tube contains a filament or cathode and a target or anode which are held within a vacuum (Bell and Nadrljanski). X-ray production is initiated by heating the filament with energy delivered through an electrical circuit to the X-ray tube. This process causes the cathode to release electrons, which are then accelerated towards the anode to produce the X-rays (Bell and Nadrljanski).

The application of this external energy source causes an electron from the inner shell of the atom to be ejected from its orbital (Guthrie, 1996). An electron from one of the outer orbitals then moves into the vacant space left by the ejected electron in the innermost orbital (Guthrie, 1996). The process of an outer shell electron dropping in energy as it moves to the inner orbital causes a small amount of radiation to emit from the inner shell of the atom (Guthrie, 1996). This emitted radiation, referred to as the secondary X-ray photon, is measured by the detector within the XRF analyzer. Detectors in energy dispersive XRF spectrometers, like the one used in this study, measure the entire spectrum of energy emitted from the sample and translate it into a histogram of the intensity or number of counts of each photon energy (Guthrie, 1996). This process is illustrated by the Olympus pXRF user manual shown in figure 2.2. The specific energies associated with these photons are characteristic of the atoms from which they came, allowing the identification of the elements present within the excited area of the sample and the quantification of the amount of each of those elements (Guthrie, 1996). An example of an

element weight percent table and spectrum produced by the pXRF are provided in figures 2.3 and 2.4 from the Olympus pXRF user manual.

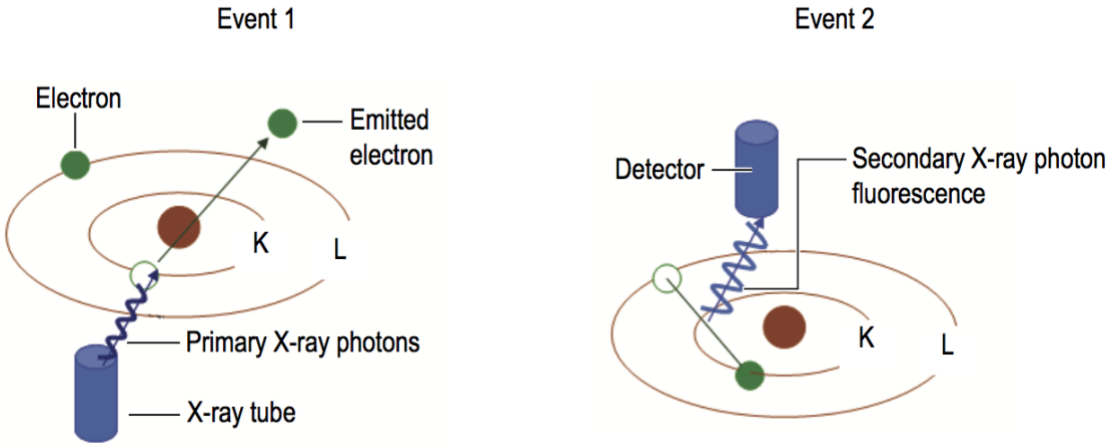

Figure 2.2: Diagram of electron ejection detection process (Olympus, 2020).

El	%	+/-
Ti	0.671	0.050
V	0.140	0.022
Cr	17.71	0.14
Mn	1.683	0.078
Fe	68.98	0.20
Co	0.514	0.093
Ni	9.35	0.14
Cu	0.218	0.031

Figure 2.3: pXRF element weight percent table (Olympus, 2020).

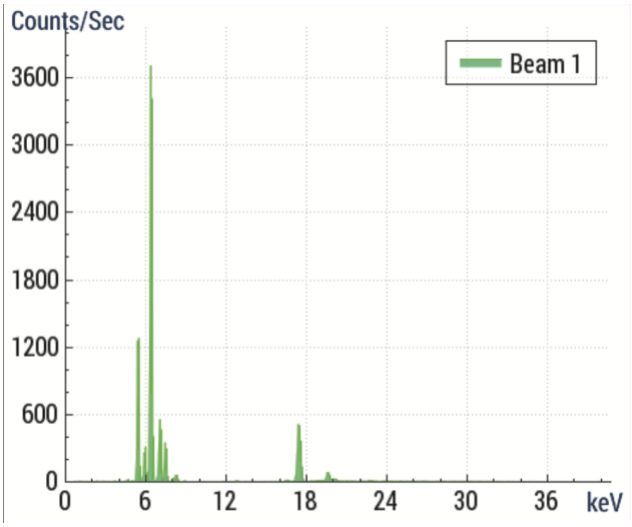

Figure 2.4: pXRF spectrum of intensity vs. energy (Olympus, 2020).

2.3 pXRF Measurement Collection

Two methods of pXRF measurement collection were used in this study. The first was a muti-spot chemical analysis, where measurements were collected at three different points located

in various areas of each sample. The second method was a single-spot chemical analysis, where measurements were collected at one individual spot of the sample and that measurement was repeated three times. These two methods were used to test the compositional homogeneity of the samples and to ensure that the collected data was consistent and reliable. Since Na is not within the detection limits of the instrument, Na_2O weight percentages were not be presented in any of these tests. In the absence of Na_2O data, specific rock types could not be deduced from the pXRF tests, however SiO_2 and K_2O data was used to determine a range of possible rock types for each sample.

Chapter 3: Results

3.1 Sample #119a-A Structural and Textural Analysis

This sample exhibits a glassy texture with both irregular and conchoidal fracturing. The flow banding structures observed in the unweathered areas of the sample are well defined, meaning they possess clean, clear boundaries. These bands have a dark grayish brown color, which comprises approximately 35% of the sample. The flow bands are bordered by a lighter, off white colored rock, which fills the area between each of the darker flow bands and dominates about 65% of the sample. The flow bands vary in thickness from approximately 1 to 4 mm and the thickness of each individual band is also ununiform, as the bands narrow and widen along their lengths. In some instances, a band may disappear entirely and then reemerge further along its length, creating a pinched-out, segmented flow band, which is shown in the band that cuts through the center of figure 3.1. These discontinuous, boudin-like structures are likely a result of shear stress. In addition to their discontinuity and varying thicknesses, these flow structures also show a wavy morphology rather than forming straight lines across the sample.

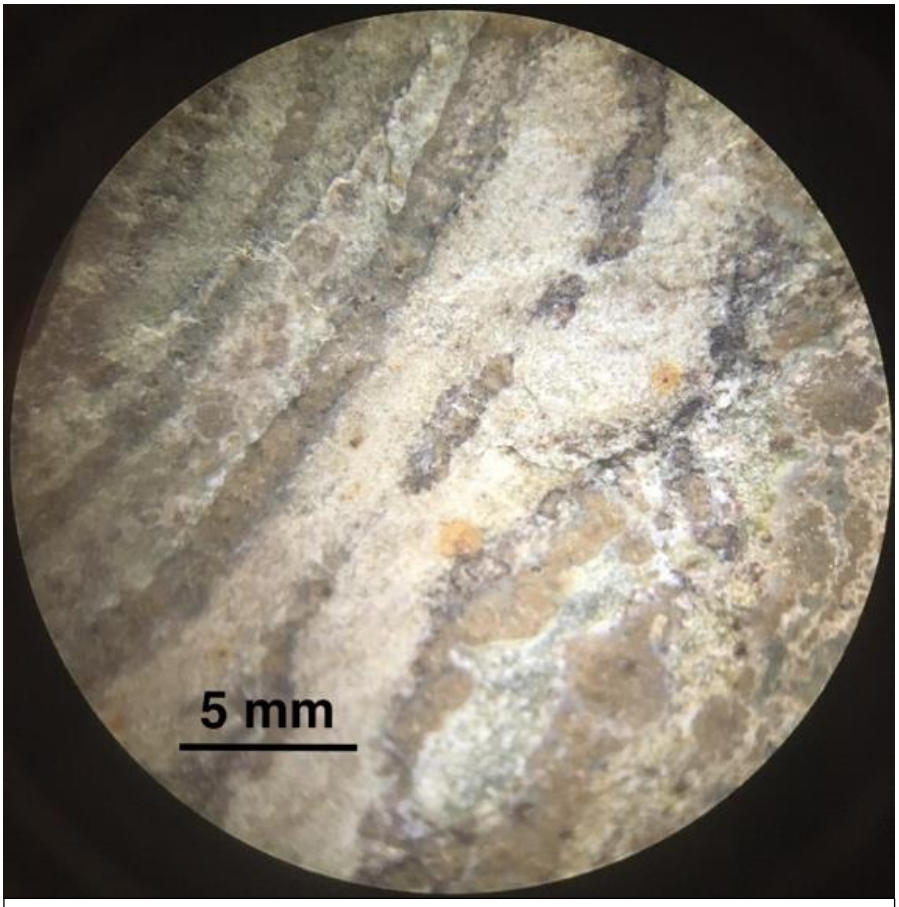

Figure 3.1: Shear-induced segmentation of flow bands in sample 119a-A

Certain isolated regions of the sample contain spherules with diameters ranging from under 0.25 to 2 mm. Images of these structures are provided in figures 3.2 and 3.3. These spherules appear as irregularly shaped, rounded grains, enclosed by under 0.25 to 0.3 mm thick white rims which outline the perimeters of the spherules. Some flow bands and spherules, like those shown in figure 3.3, are rimmed by under 0.25 mm bands of a very dark reddish-brown to black mineral. The lack of concentric circular patterns repeated within the spherules indicate that they have been subjected to a greater degree of weathering (Pollock et al., 2008). The area of space between these spherules is often filled by a matrix of smoky quartz.

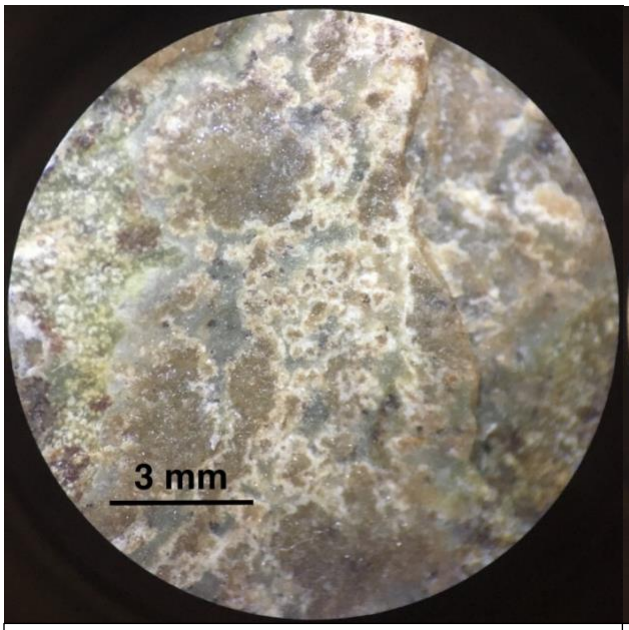

Figure 3.2: Spherules with white rims in a matrix of smoky quartz in sample 119a-A

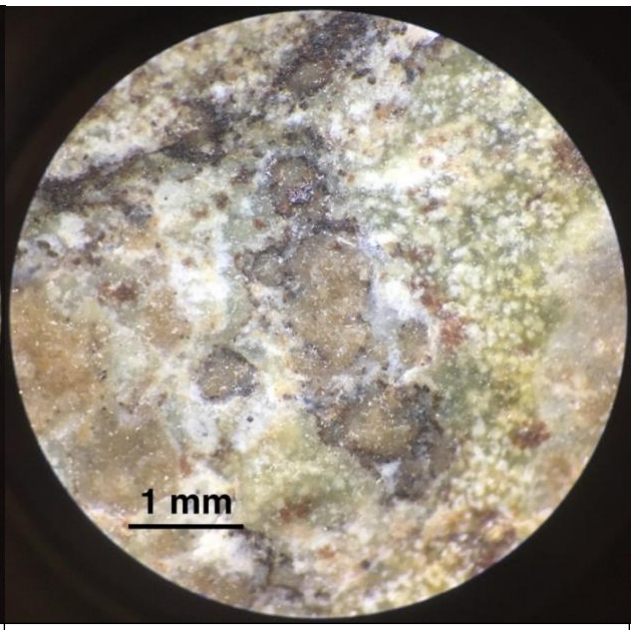

Figure 3.3: Spherules outlined by dark mineral rims in sample 119a-A

Each side of this particular hand sample exhibits a different degree of weathering. One of the more lightly weathered areas of the sample is displayed in figure 3.4, where the rock that fills the spaces between each flow band has a light green tint in place of the off-white color observed in the unweathered regions of the sample. This degree of weathering also altered the grayish-brown color of the flow bands to a slightly rustier variety. The more heavily weathered regions of this sample exhibit clouded patches of gray and rusty orange, and the flow banding is no longer visible in these areas. An area of this heavily weathered region is shown in figure 3.5.

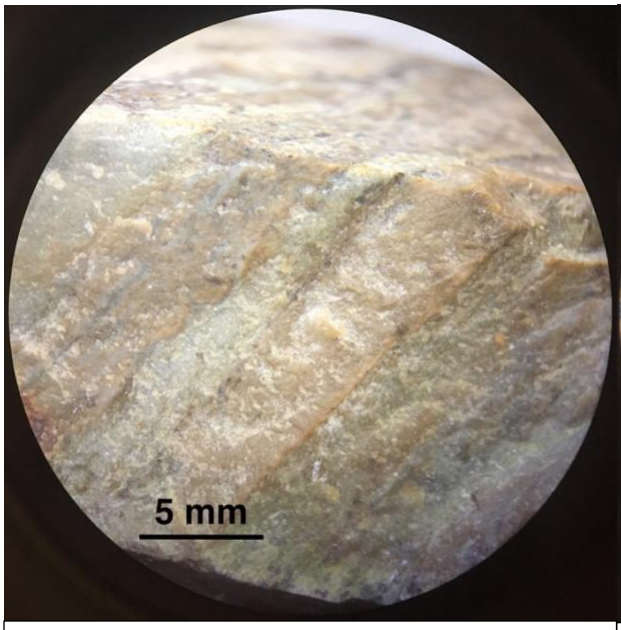

Figure 3.4: Lightly weathered surface of sample 119a-A with rusty flow bands bordered by green

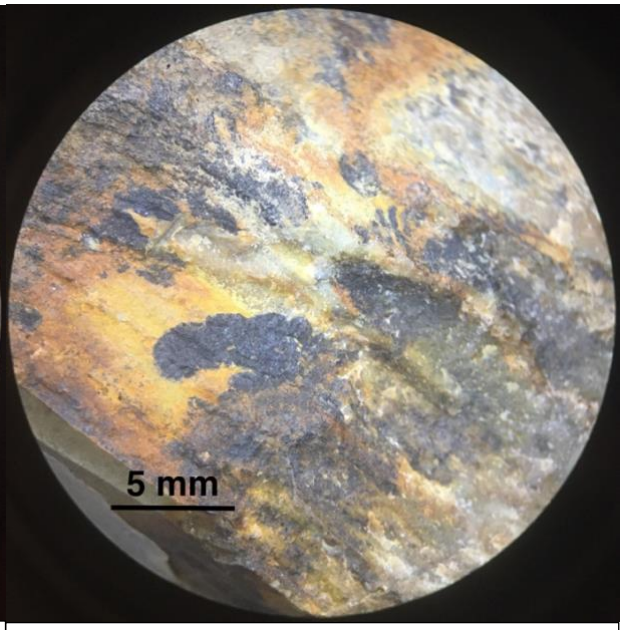

Figure 3.5: Heavily weathered surface of sample 119a-A with dark and rusty clouding

3.2 Sample #119a-B Structural and Textural Analysis

The texture of this sample is very glassy, and the vast majority of the sample shows no visible grains that would allow any sort of mineral identification. However, a few areas of the sample contain clusters of a speckly black mineral that are concentrated around the edges of the flow bands, creating dark borders which partially outline some of the flow bands, like those shown in figure 3.6. Most of these speckles have poorly defined or indistinguishable grain boundaries. These speckles or grains are under 0.25 mm in diameter. Due to the small size of these grains, their weak definition, and their lack of distinguishable crystal habit, identification of this mineral was not possible for this sample.

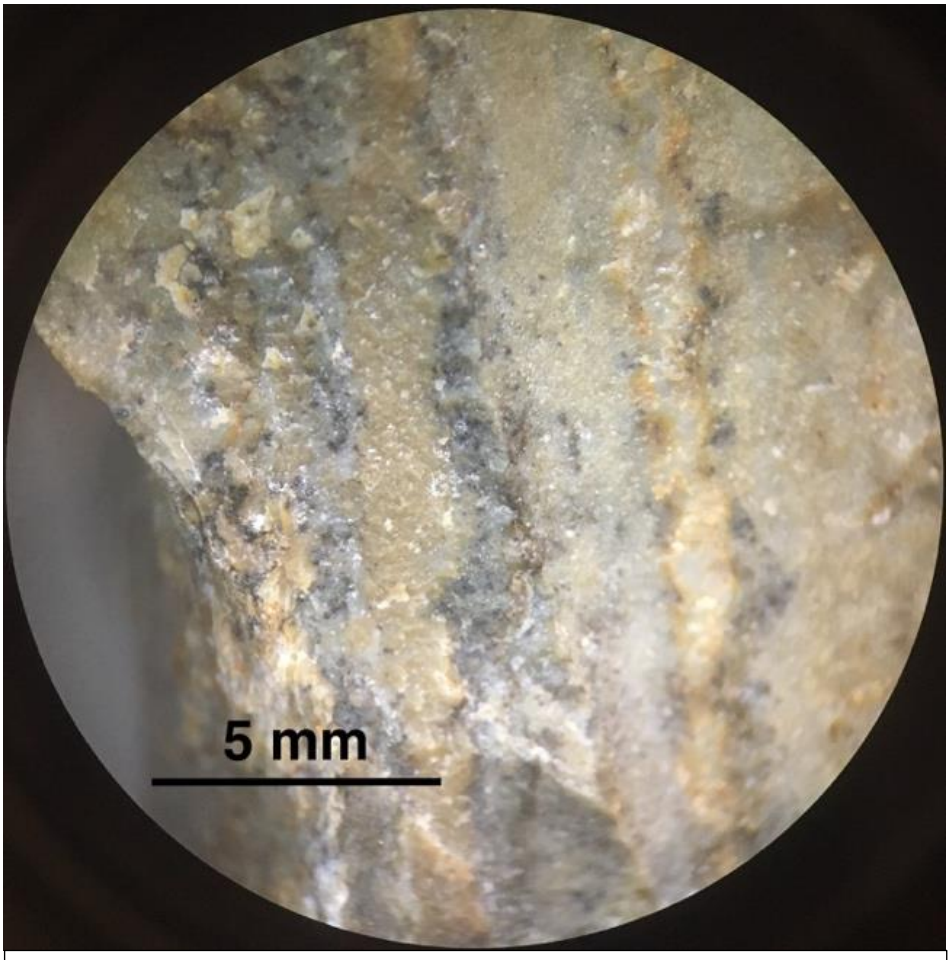

Figure 3.6: Flow banding structures outlined by a speckled black mineral in sample 119a-B

The few flow bands observed in this sample range from about 0.7 to 2 mm in width. Like sample 119a-A, the width of an individual flow band in this sample varies throughout its length, leaving each flow band with greater thicknesses in some locations along the band and lesser thicknesses in others. The varying thickness observed at different points along the length of an individual band may differ by a maximum of approximately 1.3 mm. The flow bands in this sample appear to be slightly curved, however they do not exhibit the same magnitude of waviness as sample 119a-A. Due to the slightly weathered nature of this sample, the flow bands appear as a rusty orangish-brown color, while the areas between the flow bands are filled with a

light green colored rock. A few smaller patches of the sample contain dark gray clouding, indicating that heavier weathering occurred in those areas.

3.3 Sample #119a-C Structural and Textural analysis

Like samples 119a-A and 119a-B, this sample has a glassy texture and lacks any grains large enough for mineral identification. The vast majority of the visible rock surface on this sample is covered with a relatively high degree of weathering, which obscures or eliminates the visibility of most of the flow banding present at the surface of the sample. The heavily weathered surfaces consist of rusty orange to red and grey to black clouding. In the less weathered areas where the flow banding is distinguishable, the flow bands appear as dark brown to charcoal gray colored layering with prominent to weakly pronounced definition separated by a white to greenish-gray colored rock. These variations in rock color and banding definition are a result of the differing degrees of weathering observed throughout the sample.

The widths of the flow bands range from approximately 0.7 to 4 mm and the majority of the flow bands exhibit a relatively uniform thickness throughout their length. The flow bands run straight across the sample rather than being wavy or curved, like the band morphologies observed in samples 119a-A and 119a-B. However, this sample does share a spherulitic texture similar to what was found in sample 119a-A. These spherules appear as irregularly shaped, rounded structures that range from under 0.25 to 1 mm in diameter. Like those found in sample 119a-A, these spherules are often enclosed by white or dark mineral rims. Both of these outlining structures are illustrated in figures 3.7 and 3.8 and are under 0.25 mm in thickness. In addition to the flow banding and spherule structures, this sample displays some unique shear structures that

are not present in any of the other 119a samples. These sheared flow banding structures and their associated shear sense is demonstrated in figure 3.9.

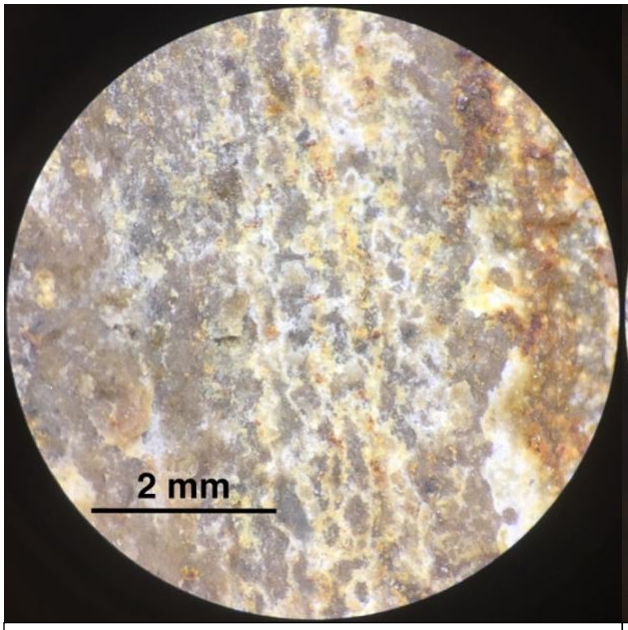

Figure 3.7: Irregularly shaped spherules enclosed by white rims within a flow band in sample 119a-C

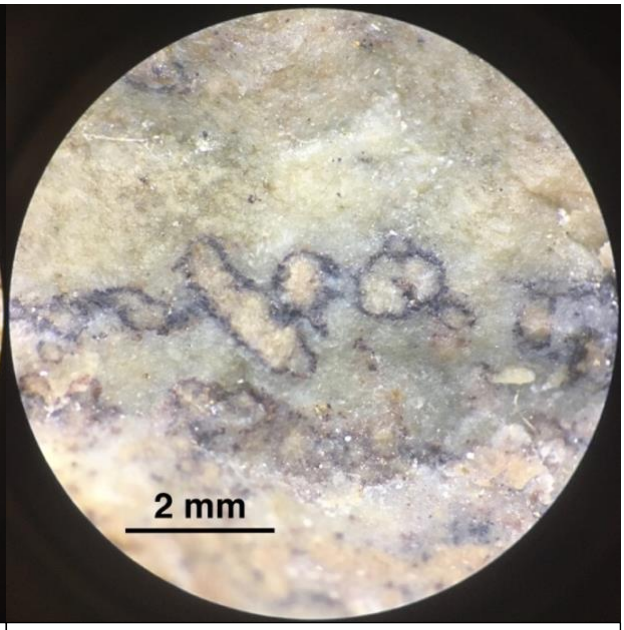

Figure 3.8: Spherules outlined by a dark mineral in sample 119a-C

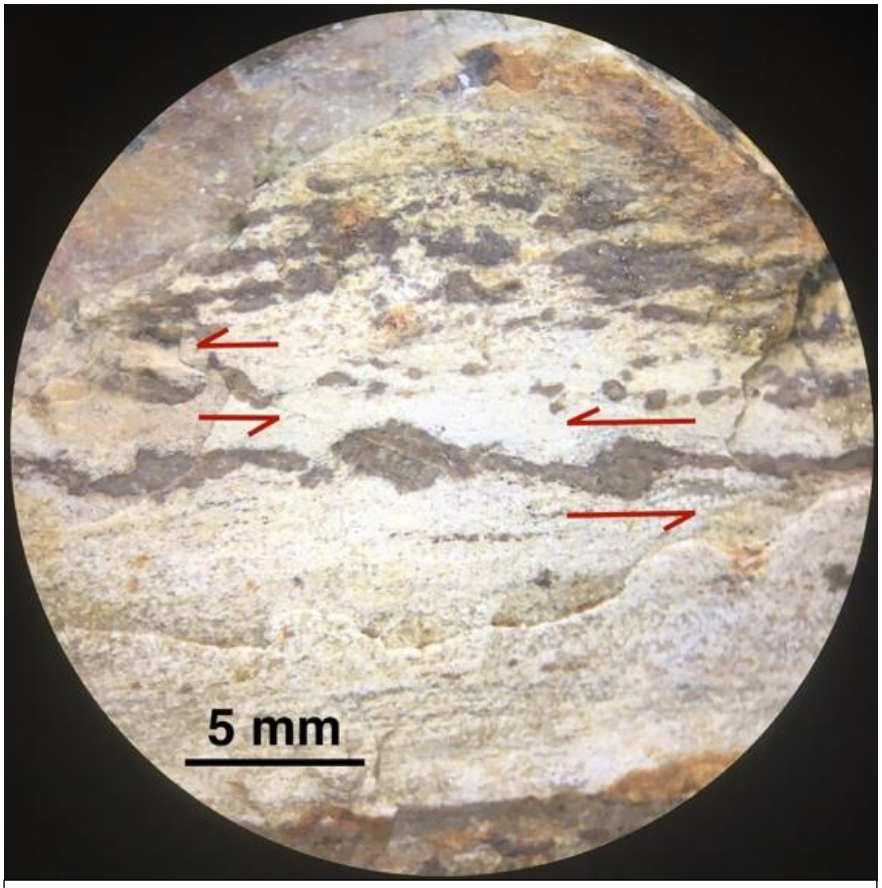

Figure 3.9: Sheared flow banding structures in sample 119a-C; red arrows indicate left-handed shear sense

3.4 Sample #119a-D Structural and Textural analysis

Unlike the other 119a samples, this sample is covered entirely by heavily weathered surfaces. Due to this great degree of weathering, there are absolutely no flow banding structures or spherules visible within this sample. Similar to what was observed in the weathered areas of the previous samples, about 15% of sample 119a-D displays areas of glassy light to mid-toned green rock, approximately 9% is comprised of very dark gray to black weathering, and about 6% of the surface is covered with rusty orange to red clouding. The remaining 70% of the sample displays a mid-toned grayish-brown colored weathering.

3.5 Dike 119a

Overall, dike 119a exhibits a glassy texture with a mixture of unweathered to light green, rusty and gray to black clouding on its more heavily weathered surfaces. This dike possesses well defined 0.7 to 4 mm dark gray to brown flow banding bordered by off white rock. The darker bands may be locally segmented or sheared and have wavy to slightly curved morphologies with ununiform thicknesses. Certain bands may also be rimmed with thin dark mineral bands. The dike also possesses under 0.25 to 2 mm spherules confined to its darker flow bands. Many of these spherules also exhibit white or dark mineral rims.

3.6 Sample #121-A Structural and Textural analysis

This sample has a glassy texture which contains no visible grains for mineral identification. About half of the surface area of the sample remains unweathered. In these areas, the flow bands appear as a dark, chocolaty brown color and the rock which comprises the negative space that exists between the flow bands is characterized by a milky beigeish-white color. These darker colored flow banding structures cover about 40% to 50% of the sample, while the lighter colored rock dominates the remaining area. Each flow band is very well pronounced and runs in a straight-line formation across the sample. The thicknesses of these flow bands range from under 0.25 mm to 1 mm. The thicknesses appear to be relatively uniform along the length of the individual bands, however they behave in a slightly different manner than those seen in the other samples. At first glance, many of these bands appear to be thicker, 0.5 to 1 mm bands, but upon closer examination, it was revealed that many of these wider bands are actually composed of a series of much narrower under 0.25 mm bands. In certain areas along the flow bands, these thinner bands are separated and distinguishable from one another, but further

along the band, they resolve into one wider cohesive flow band. All of these characteristics are illustrated in the photograph of the flow banding provided in figure 3.10.

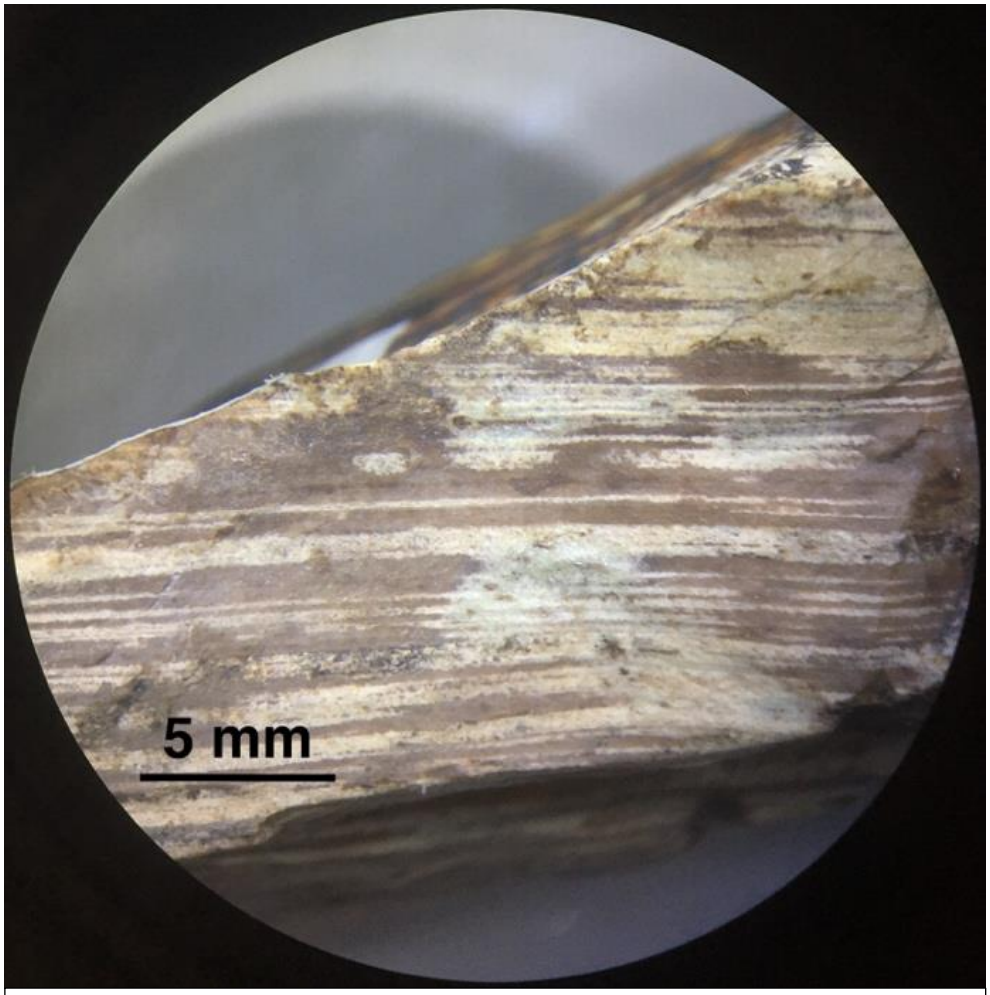

Figure 3.10: Resolving of individual narrow flow bands into larger cohesive bands in sample 121-A. Flow banding is dark and very well defined.

Sample 121-A does not display any additional spherulite or shear structures as some of the other samples do, however it does possess many similar weathering characteristics. The sample displays smooth areas of light green weathering, which amplify its glassy texture as well as areas of black and rusty colored clouding. The sample also contains areas of speckly black weathering in addition to clusters of 1.5 to 6 mm tall pillars of black weathering that divide into several outreaching branches, which line some of the edges of the sample. Each of these varieties of weathered surfaces are shown in the sample images provided in figures 3.11 and 3.12.

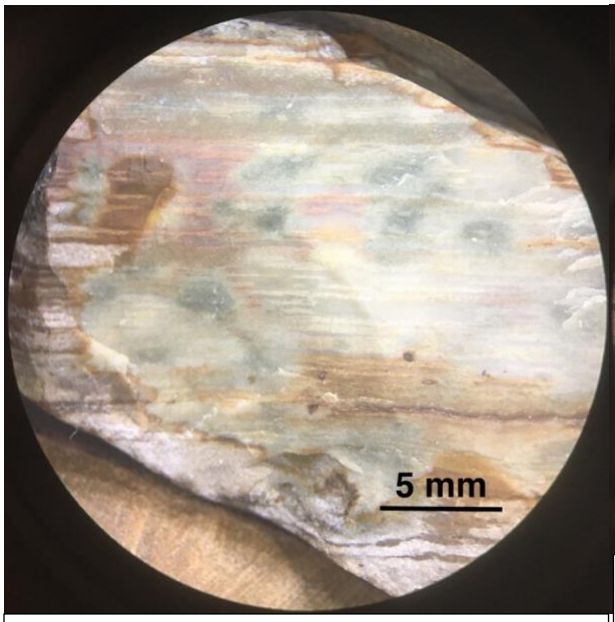

Figure 3.11: Light green weathering and rusty clouding of flow bands in sample 121-A

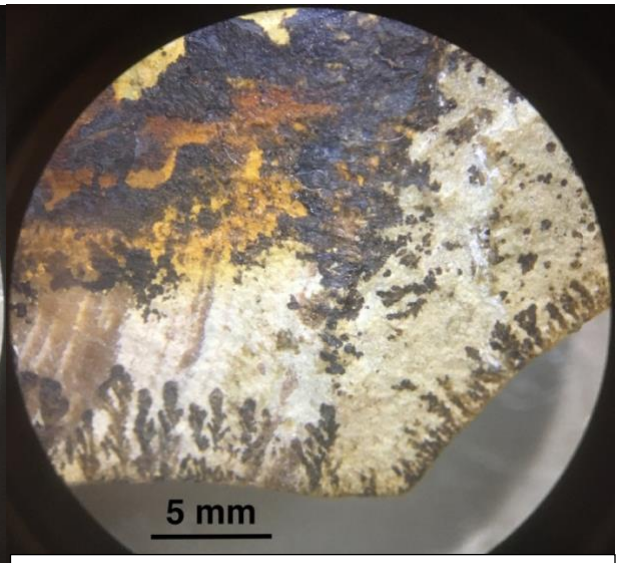

Figure 3.12: Black and rusty clouding in the upper left region of the figure, black speckled weathering on the right, and branching pillars of dark weathering lining the bottom edges of the sample.

3.7 Sample #121-B Structural and Textural analysis

Like sample 121-A, this sample has a glassy texture and lacks any visible grains. About 80% of the sample's surface is heavily weathered, eliminating any visibility of the flow banding structures. The remaining 15% of the sample displays a lesser degree of weathering, which obscures the appearance of the flow banding, but does not hide it completely. In these more visible areas, the banding is not unlike what was observed in sample 121-A. The flow bands range from under 0.25 mm to 1 mm in width and follow the same coalescing and dividing patterns with straight-line morphologies. The color and definition of the flow bands are weakened by the weathering, as the sharp, dark brown color of the flow banding has been altered to a much lighter, poorly pronounced, hazy brown color. An image of this visually obscured flow banding is provided in figure 3.13. The remaining heavily weathered surfaces of the sample display very dark brown to black clouding and speckled weathering, rusty clouding, and

outreaching sprays of black weathering, similar to the weathered surfaces observed along the edges of sample 121-A in figure 3.12.

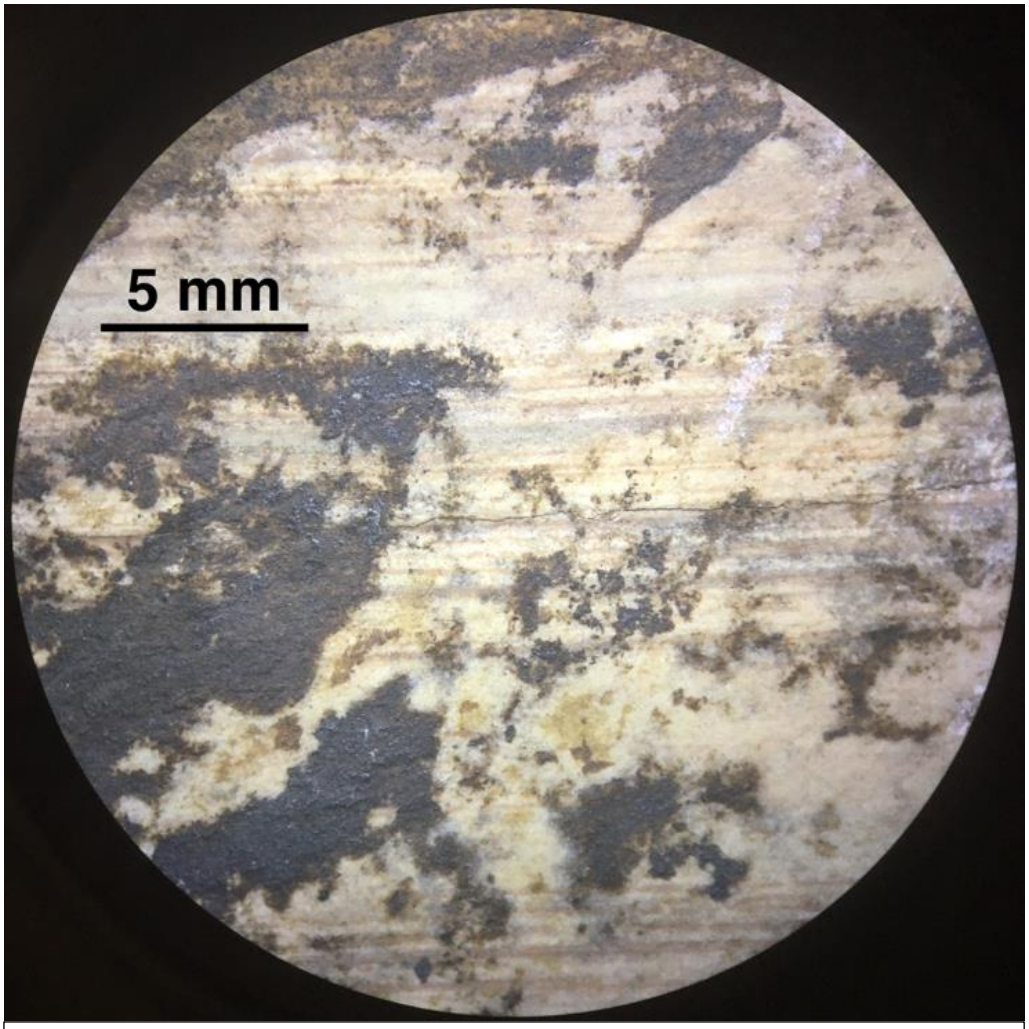

Figure 3.13: Flow banding obscured by hazy weathering and black clouding on the surface of sample 121-B

3.8 Sample #121-C Structural and Textural analysis

This sample also possesses a glassy texture with no identifiable mineral grains. It is similar to sample 121-B in that the vast majority of its surface is dominated by heavy weathering. About 10% of the sample's surface area remains completely unweathered. Within this small area are moderately to poorly pronounced, brown to light gray flow bands bordered by

white rock. These flow banding structures range from approximately 0.7 to 1.5 mm in width and display continuous, uniform thicknesses throughout each band. An image of this unweathered area of the sample, where the flow banding is visible, is provided in figure 3.14. These flow bands run in straight lines across the sample and show some instances of banding cohesion and separation, however this pattern is not as commonly observed in this sample as in samples 121-A and 121-B. The flow banding structures comprise about 30% of the sample, while the remaining 70% is composed of the milky white colored rock that fills the space between the flow bands.

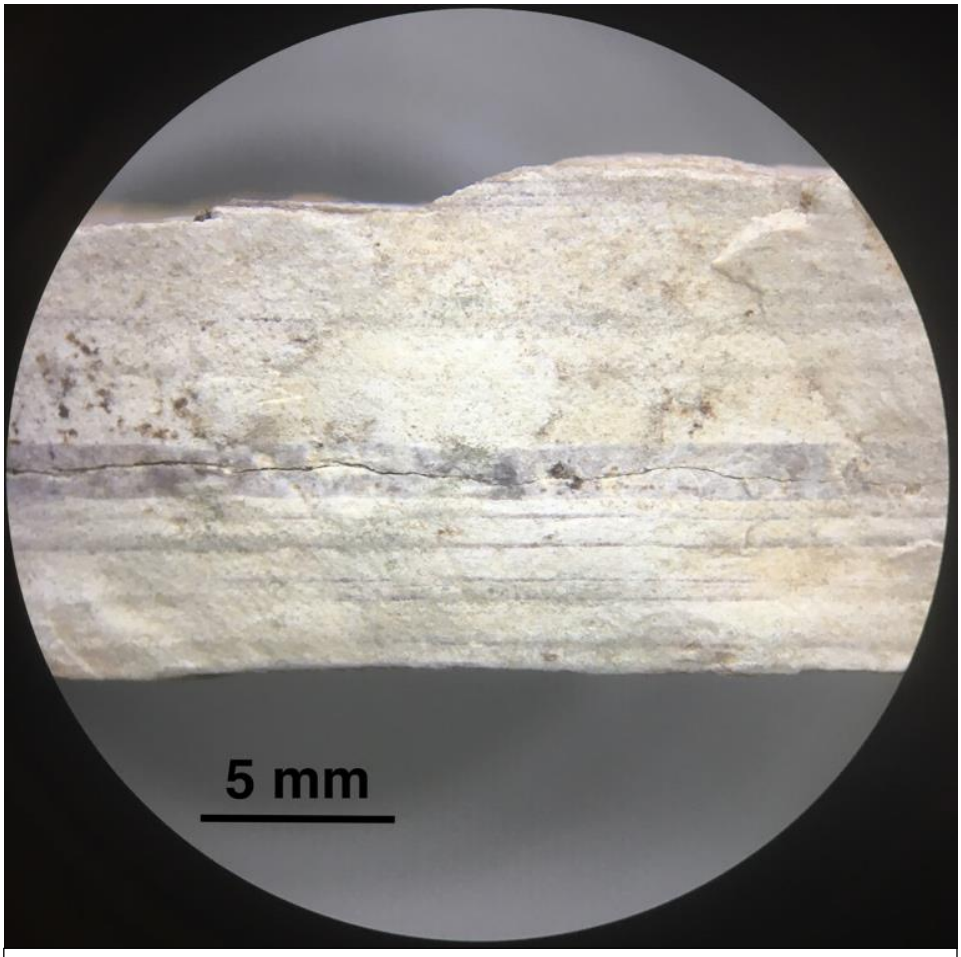

Figure 3.14: Unweathered surface of sample 121-C with poorly pronounced flow banding

Sample 121-C displays some interesting weathered surfaces, some of which are not found in any of the other nine samples. One half of this sample, shown in figure 3.15, is dominated by

very dark brown to black and greenish-brown patchy clouding, which is unique to this sample. The other side of the sample, illustrated in figure 3.16, is primarily covered with a greenish-brown clouding that fades into a very light green weathering. This weathered region is also outlined with a band of rusty weathering. Some of this area is also overlain by a network of opaque, grayish-black weathering.

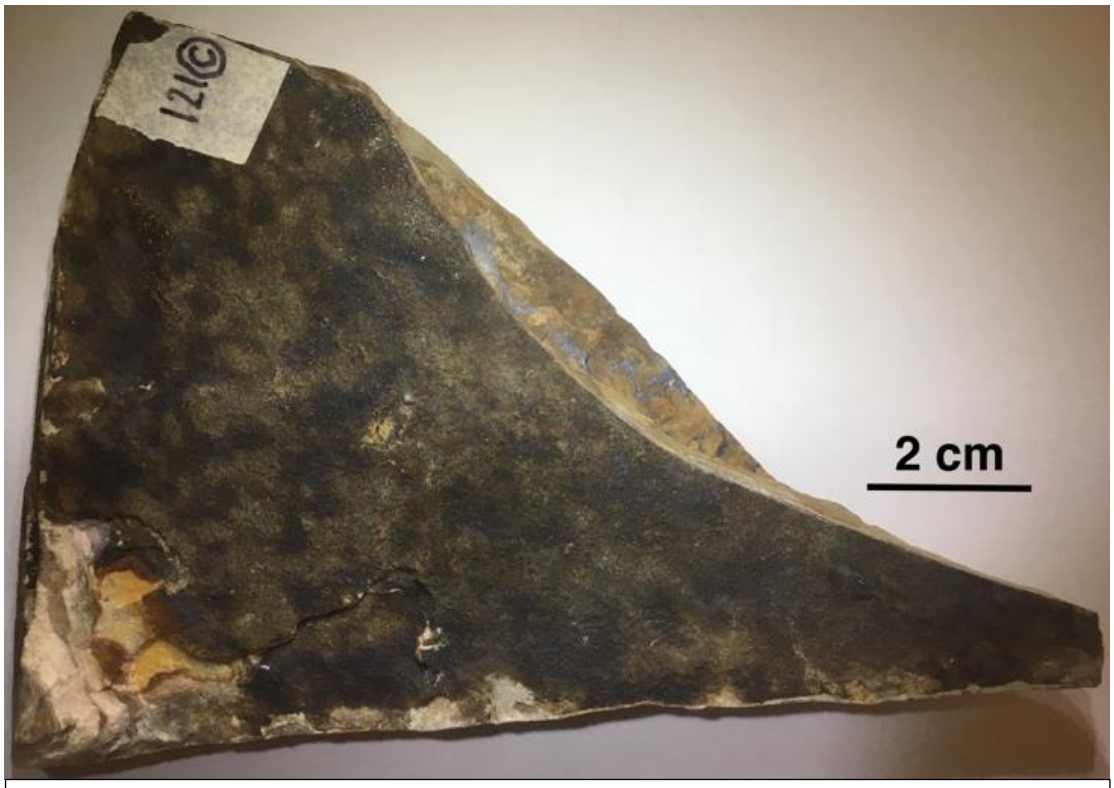

Figure 3.15: Weathered surface of sample 121-C with dark, patchy clouding

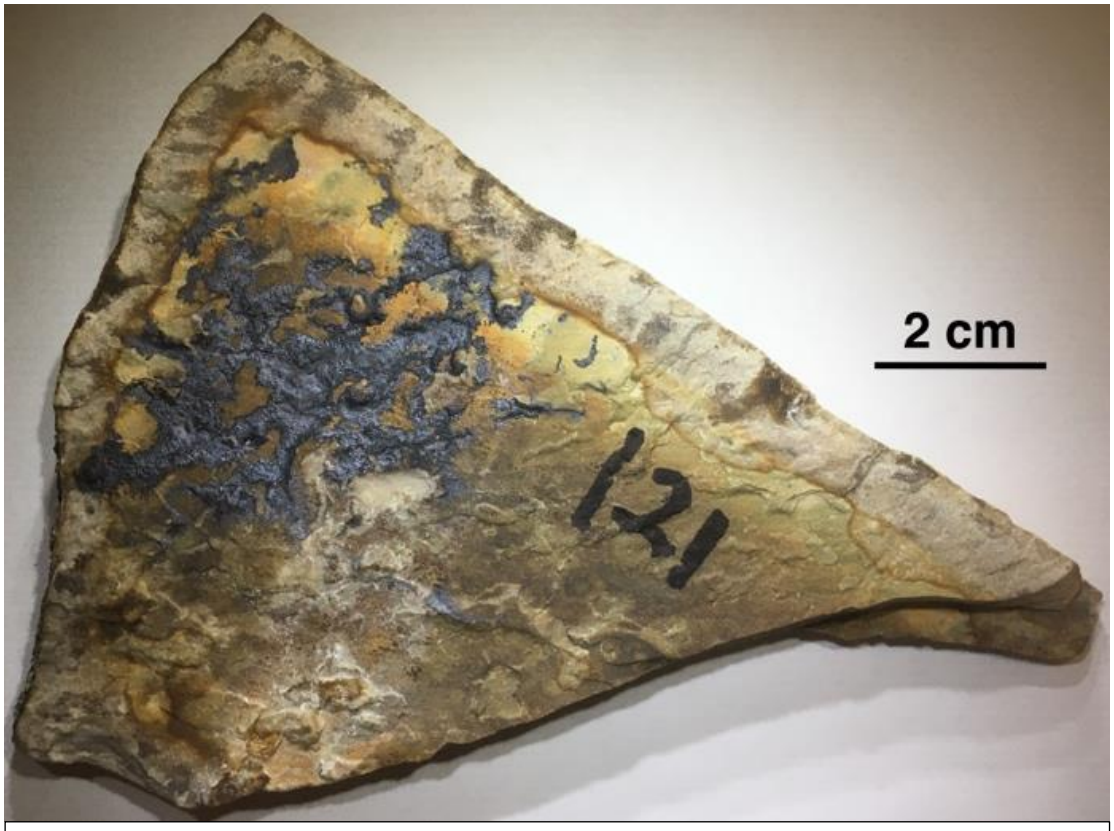

Figure 3.16: Brown, green, rusty and opaque black weathered surfaces of sample 121-C

3.9 Dike 121

Overall, dike 121 possesses a glassy texture with a mixture of unweathered to light green, rusty, milky and black clouding and black speckled weathering. Dike 121 exhibits well defined dark brown banding as well as poorly defined light brown to beige flow banding bordered by a milky off-white colored rock. The flow banding ranges from under 0.25 to 1.5 mm thickness and exhibits a straight band morphology with a separating and resolving pattern.

3.10 Sample #123 Structural and Textural analysis

Sample 123 is extremely glassy and contains no visible grains. Relative to all of the other nine samples, this sample displays the glassiest texture. Although half of the sample's surface is somewhat heavily weathered, the flow banding is visible throughout the entirety of the sample.

The less weathered flow bands, shown in figure 3.17, appear as very poorly pronounced very light green to white bands that range from approximately 0.25 to 0.7 mm in width. The bands run in a straight line across the sample but appear to show some very slight variations in thickness along many of the individual bands. In other words, the individual band thickness is not quite uniform. The rock that fills the space between the bands has a mid-toned grayish-green color and dominates about 65% of the sample, while the remaining 35% is composed of the previously described lighter green to white flow banding. On the more heavily weathered side of the sample, shown in figure 3.18, these darker grayish-green areas have been altered to a dark gray color, while the lighter green to white flow banding appears as a light gray weathered color. This pattern of alternating dark and light gray bands is then overlain with a small amount of black and rusty-brown clouding.

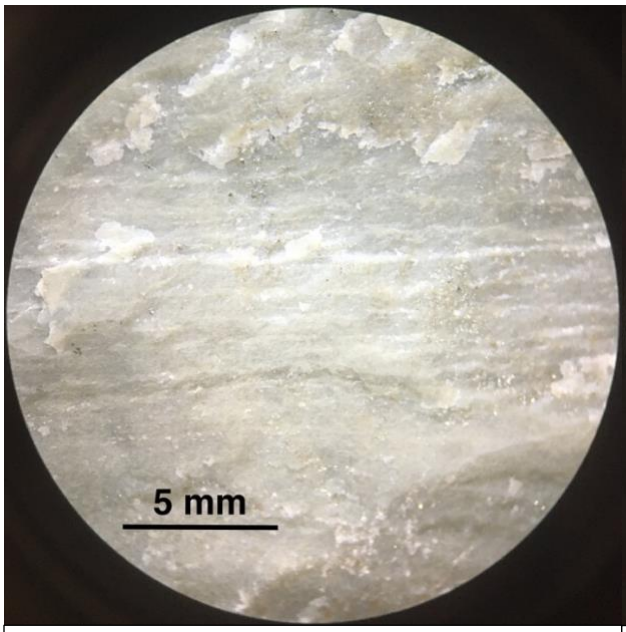

Figure 3.17: Lightly weathered surface of sample 123 with very light green, weakly pronounced flow bands bordered by darker green glass

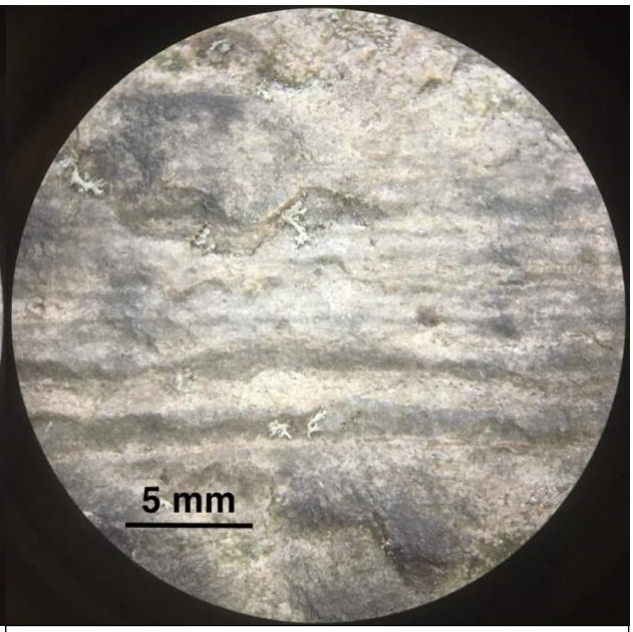

Figure 3.18: Heavily weathered surface of sample 123 with alternating bands of light gray weathered flow bands bordered by dark gray weathered rock

3.11 Sample #34 Structural and Textural analysis

Sample 34 displays porphyritic texture with some larger 0.5 to 4 mm phenocrysts. The ground mass appears to be primarily composed of transparent to white quartz and white to yellowish-white plagioclase, although the grain boundaries between these two varieties of mineral grains are highly difficult to distinguish in most areas of the groundmass, even when observed at maximum (35x) magnification under the binocular microscope. The plagioclase and quartz grains found in the groundmass generally range from less than 0.25 mm to 0.5 mm in diameter. The final mineral present in the groundmass is a dark gray to black mineral with a hardness of approximately 2 to 4 on the Mohs hardness scale, which appears in under 0.25 mm black grains. These dark grains comprise approximately 15% of the groundmass, while plagioclase and quartz dominate the remaining 85%. Because of the lack of clearly defined grain boundaries between the plagioclase and quartz grains, the identification of the proportions of each of these minerals in the groundmass is not possible. A magnified image of the groundmass and its compositional mineral grains is provided in figure 3.19.

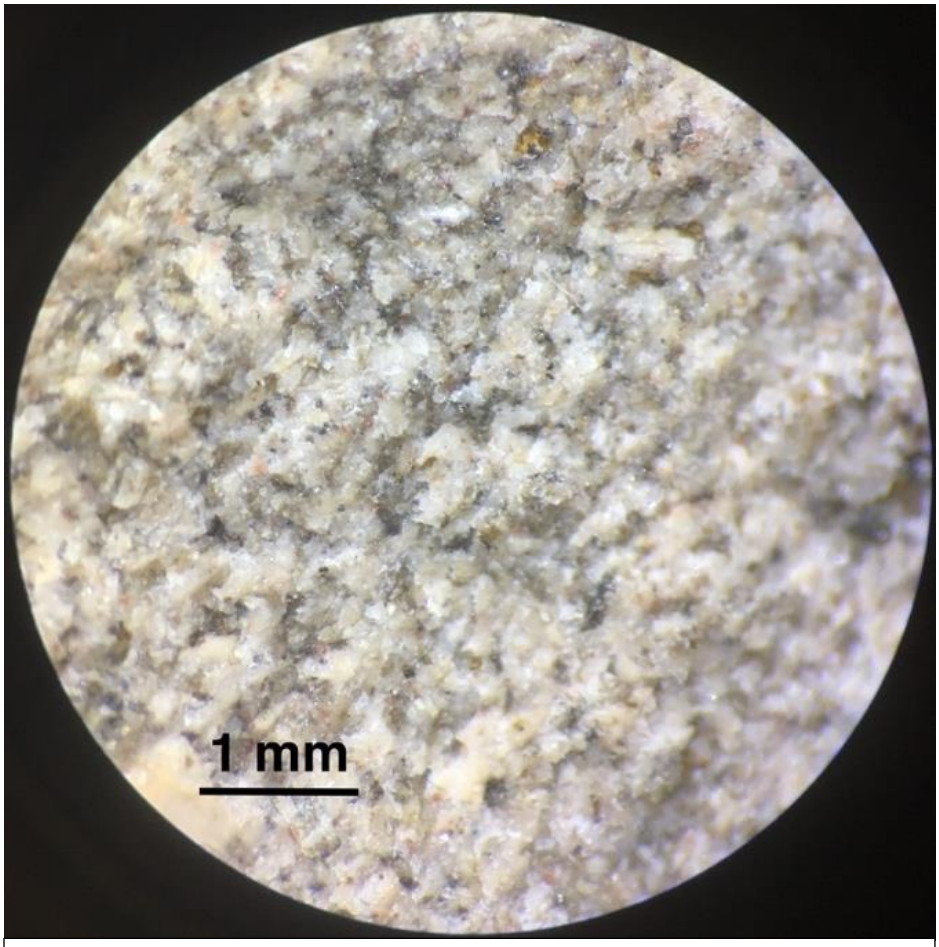

Figure 3.19: Sample 34 groundmass composed of quartz (transparent/white), plagioclase (yellowish-white), and dark gray to black mineral grains.

The phenocrysts observed in this sample make up about 5% of the entire sample, while the remaining 95% is composed of groundmass. These phenocrysts include both 0.5 to 4 mm yellowish white, blocky plagioclase grains which are shown in figure 3.20, as well as 0.5 to 2.5 mm dark gray to black mineral grains, shown in figure 3.21. The dark mineral grains comprise about 10% of the sample's total phenocrysts, while plagioclase dominates the remaining 90%. There are no flow bands or spherulite structures present within this sample, however it does display some dark greyish-brown weathering on about half of the sample's surface.

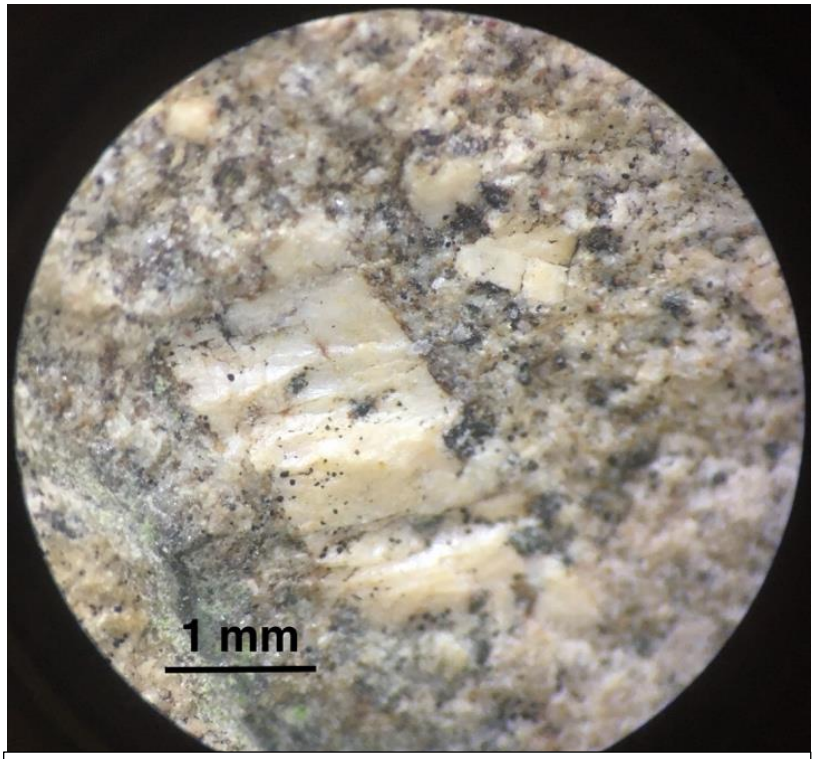

Figure 3.20: Blocky plagioclase phenocryst in sample 34

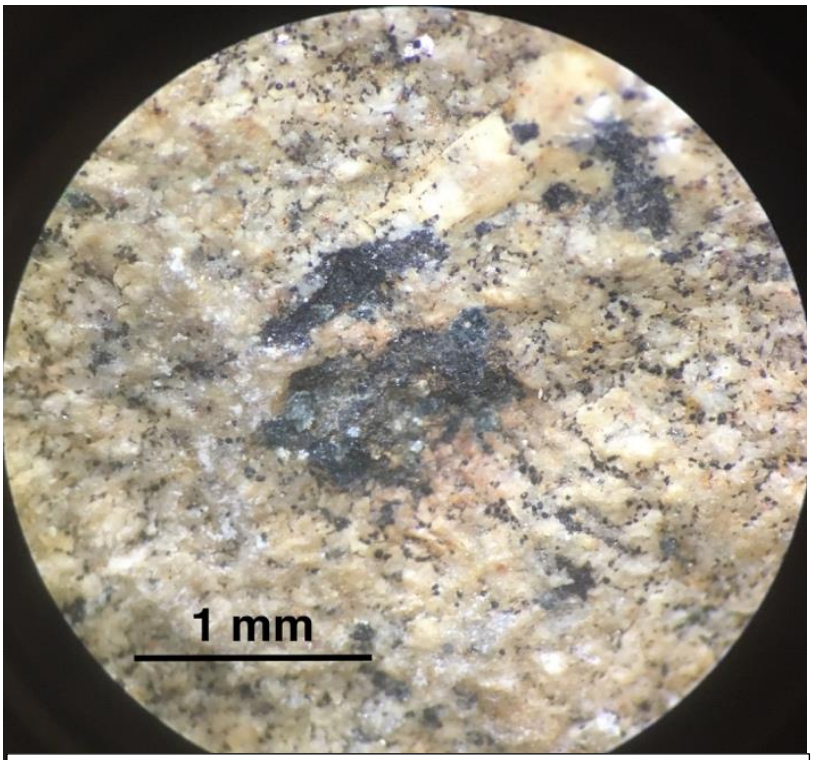

Figure 3.21: Dark mineral phenocryst in sample 34

3.12 Sample #27b Structural and Textural analysis

This sample has a porphyritic texture, with most of the sample being made up of a very fine-grained crystalline groundmass. About 95% of the groundmass is composed of a salmon pink microcrystalline rock and 5% is made up of small brownish-red grains which measure to be under 0.25 mm in diameter. Both of these components can be seen in the photograph of the groundmass provided in figure 3.22. Minerals present within the groundmass are unidentifiable due to their very small size. About 2% of the entire sample is made up of tiny phenocrysts that can be identified using a binocular microscope. Approximately 60% of these phenocrysts are 0.3 to 2 mm translucent to white quartz grains, like the grain shown in figure 3.23. The remaining 40% of the phenocrysts are dark red to metallic gray 0.25 to 1.5 mm grains with a hardness of about 2 to 4, like those shown in figure 3.23 and 3.24. Like sample 34, this sample is unlike most of the other samples, as it does not contain any flow banding or spherulite structures, however it does show some light-gray clouding that can be found in many of the other samples.

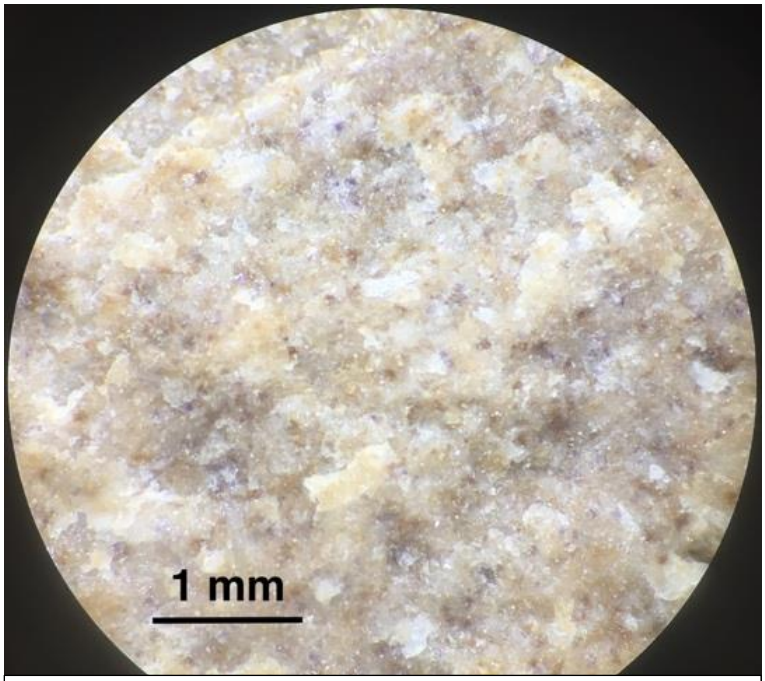

Figure 3.22: Groundmass of sample 27b with pink glass and dark speckled grains

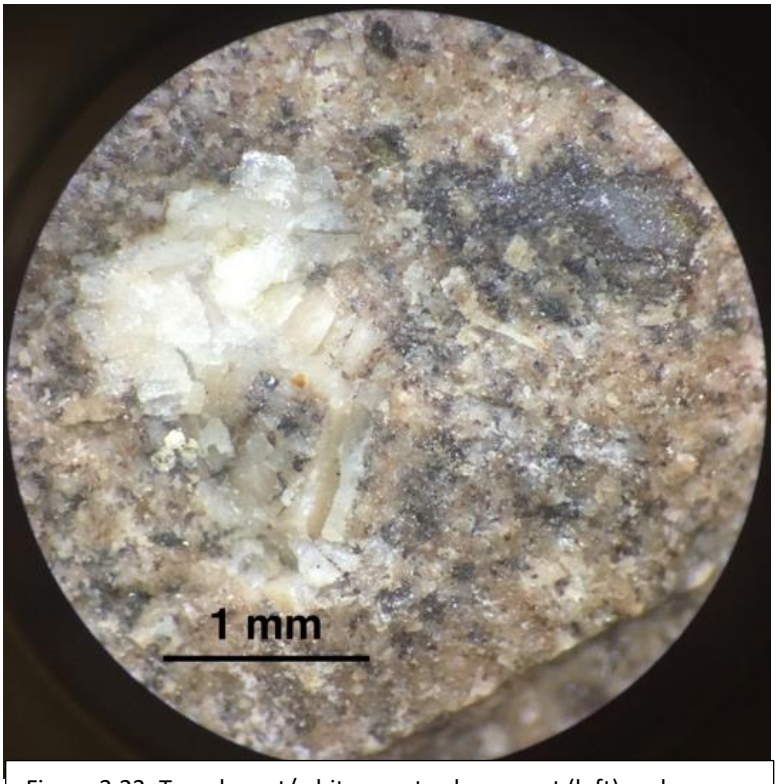

Figure 3.23: Translucent/white quartz phenocryst (left) and metallic gray phenocryst (right) in sample 27b

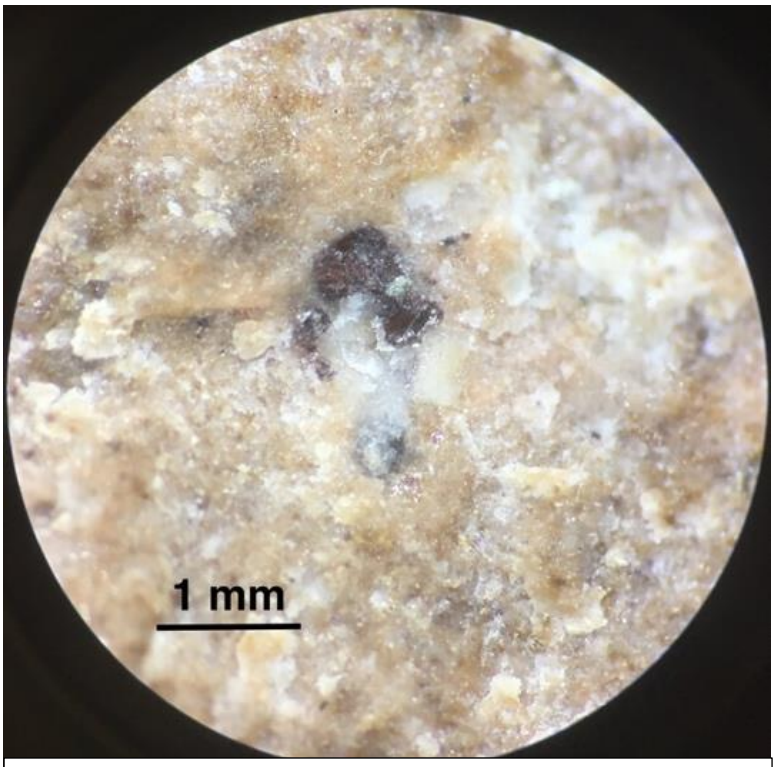

Figure 3.24: Dark red phenocryst in sample 27b

3.13 Chemical Analysis

Tables 3.1-3.7 summarize the results from pXRF chemical analyses completed for samples 119a-A, 119a-B, 119a-D, 121-A, 123, 34 and 27b. The remaining four samples were not analyzed, because they lacked any unweathered surfaces large enough to cover the entire measurement window of the instrument. Each table includes oxide weight percentages calculated for the three multi-spot analyses, which are listed in red, as well as for the three single spot analyses, which are listed in blue. Note that the results from each of these six tests are representative of the bulk composition of a ~4 square cm area of the sample that remained within the measurement window of the pXRF at the time of the test. The three multi-spot analysis tests were collected from three different areas of the sample, while the single-spot analysis tests were collected with three repeated measurements of one individual area within the sample. Also note that all weight percentages of Na_2O are listed as "n.d." (not determined), as the instrument used in this study was not capable of measuring Na. Some other weight percent measurements are listed as "<d.l." (below detection limits), which indicate that the cation is below the detection limits of the instrument for that particular sample or measurement.

Sample #123

Oxide	wt% spot 1	wt% spot 2	wt% spot 3	wt% test 1	wt% test 2	wt% test 3
SiO_2	73.29	70.02	66.28	71.03	73.74	72.14
TiO_2	0.14	0.13	0.13	0.12	0.10	0.10
Al_2O_3	13.25	12.68	12.92	12.22	12.39	12.41
FeO	1.43	1.55	1.59	1.52	1.54	1.53
MnO	0.06	0.07	0.08	0.08	0.08	0.08
MgO	>d.l.	>d.l.	>d.l.	>d.l.	>d.l.	>d.l.
CaO	0.30	0.25	0.37	0.37	0.33	0.37
Na_2O	n.d.	n.d.	n.d.	n.d.	n.d.	n.d.
K_2O	6.14	6.09	4.84	4.84	4.86	4.97
Total:	94.62	90.49	87.71	90.18	93.04	91.60

Table 3.1: Oxides and oxide weight percents calculated for multi-spot analyses (red) and single spot analyses (blue) completed for sample 123

Sample #27b

Oxide	wt% spot 1	wt% spot 2	wt% spot 3	wt% test 1	wt% test 2	wt% test 3
SiO_2	38.49	60.22	55.58	53.89	58.21	58.32
TiO_2	0.30	0.57	0.56	0.44	0.44	0.47
Al_2O_3	9.16	15.87	14.83	13.77	15.32	15.27
FeO	4.62	5.08	5.14	4.94	5.06	5.04
MnO	0.31	0.27	0.25	0.28	0.28	0.28
MgO	>d.l.	>d.l.	>d.l.	>d.l.	>d.l.	>d.l.
CaO	14.69	>d.l.	3.22	1.93	2.08	2.05
Na_2O	n.d.	n.d.	n.d.	n.d.	n.d.	n.d.
K_2O	2.68	6.12	4.29	4.78	5.21	5.21
Total:	70.26	88.13	83.87	80.03	86.60	86.64

Table 3.2: Oxides and oxide weight percents calculated for multi-spot analyses (red) and single spot analyses (blue) completed for sample 27b. Note that deviation of single-spot analysis test 1 is likely sourced from human error during the measurement collection.

Sample #34

Oxide	wt% spot 1	wt% spot 2	wt% spot 3	wt% test 1	wt% test 2	wt% test 3
SiO_2	58.36	64.97	61.40	58.62	62.17	63.02
TiO_2	0.42	0.40	0.32	0.39	0.35	0.38
Al_2O_3	12.89	14.25	13.25	12.72	13.23	13.91
FeO	2.68	2.06	2.07	2.28	2.18	2.27
MnO	0.10	0.06	0.07	0.09	0.09	0.09
MgO	>d.l.	>d.l.	>d.l.	>d.l.	>d.l.	>d.l.
CaO	>d.l.	>d.l.	0.05	>d.l.	>d.l.	>d.l.
Na_2O	n.d.	n.d.	n.d.	n.d.	n.d.	n.d.
K_2O	4.62	4.35	4.15	4.2	4.28	4.39
Total:	79.07	86.09	81.31	78.3	82.30	84.06

Table 3.3: Oxides and oxide weight percents calculated for multi-spot analyses (red) and single spot analyses (blue) completed for sample 34

Sample #119a-A

Oxide	wt% spot 1	wt% spot 2	wt% spot 3	wt% test 1	wt% test 2	wt% test 3
SiO_2	84.10	77.94	82.54	82.81	81.62	82.17
TiO_2	0.12	0.12	0.09	0.12	0.09	0.13
Al_2O_3	6.78	7.48	6.92	8.31	7.97	7.78
FeO	1.44	1.60	1.49	1.31	1.34	1.35
MnO	0.05	0.05	0.05	0.05	0.05	0.05
MgO	>d.l.	>d.l.	>d.l.	>d.l.	>d.l.	>d.l.
CaO	>d.l.	>d.l.	>d.l.	>d.l.	>d.l.	>d.l.
Na_2O	n.d.	n.d.	n.d.	n.d.	n.d.	n.d.
K_2O	2.14	1.90	1.92	1.82	1.54	1.89
Total:	94.63	89.09	93.01	94.42	92.61	93.37

Table 3.4: Oxides and oxide weight percents calculated for multi-spot analyses (red) and single spot analyses (blue) completed for sample 119a-A

Sample #119a-B

Oxide	wt% spot 1	wt% spot 2	wt% spot 3	wt% test 1	wt% test 2	wt% test 3
SiO_2	71.3	67.62	69.72	71.22	71.15	70.68
TiO_2	0.13	0.13	0.14	0.12	0.14	0.13
Al_2O_3	13.25	11.34	12.96	13.64	13.64	13.13
FeO	1.59	1.80	1.33	1.64	1.73	1.70
MnO	0.07	0.09	0.06	0.07	0.10	0.09
MgO	>d.l.	>d.l.	>d.l.	>d.l.	>d.l.	>d.l.
CaO	0.28	0.42	0.55	0.36	0.44	0.42
Na_2O	n.d.	n.d.	n.d.	n.d.	n.d.	n.d.
K_2O	3.38	4.21	4.80	3.28	3.30	3.21
Total:	90.00	85.61	89.56	90.28	90.50	89.36

Table 3.5: Oxides and oxide weight percents calculated for multi-spot analyses (red) and single spot analyses (blue) completed for sample 119a-B

Sample #119a-D

Oxide	wt% spot 1	wt% spot 2	wt% spot 3	wt% test 1	wt% test 2	wt% test 3
SiO_2	63.79	59.52	59.79	74.3	75.54	66.81
TiO_2	0.13	0.10	0.10	0.10	0.15	0.11
Al_2O_3	12.41	10.58	10.98	11.83	11.83	10.73
FeO	1.73	1.68	1.51	1.65	1.68	1.63
MnO	0.12	0.16	0.07	0.08	0.07	0.08
MgO	>d.l.	>d.l.	>d.l.	>d.l.	>d.l.	>d.l.
CaO	>d.l.	>d.l.	>d.l.	>d.l.	>d.l.	>d.l.
Na_2O	n.d.	n.d.	n.d.	n.d.	n.d.	n.d.
K_2O	>d.l.	0.12	>d.l.	0.96	0.89	1.00
Total:	78.18	72.16	72.45	88.92	90.16	80.36

Table 3.6: Oxides and oxide weight percents calculated for multi-spot analyses (red) and single spot analyses (blue) completed for sample 119a-D

Sample #121-A

Oxide	wt% spot 1	wt% spot 2	wt% spot 3	wt% test 1	wt% test 2	wt% test 3
SiO_2	61.23	65.70	62.21	65.10	63.09	62.47
TiO_2	0.13	0.14	0.12	0.17	0.15	0.13
Al_2O_3	19.39	17.19	18.37	18.88	18.80	19.05
FeO	2.16	1.75	1.69	2.05	2.21	2.10
MnO	0.15	0.11	0.12	0.12	0.12	0.13
MgO	>d.l.	>d.l.	1.82	>d.l.	>d.l.	>d.l.
CaO	>d.l.	>d.l.	>d.l.	>d.l.	>d.l.	>d.l.
Na_2O	n.d.	n.d.	n.d.	n.d.	n.d.	n.d.
K_2O	6.36	6.46	4.81	6.79	6.5	5.97
Total:	89.42	91.35	89.14	93.11	90.87	89.85

Table 3.7: Oxides and oxide weight percents calculated for multi-spot analyses (red) and single spot analyses (blue) completed for sample 121-A. Note that deviation of single-spot analysis test 1 is likely sourced from human error during the measurement collection.

According to these tests, the silica contents of these samples generally range from approximately 54 to 84%, which are characteristic of intermediate to felsic compositions. Samples 123, 119a-A and 119a-B possess strictly felsic compositions, while samples 27b, 34 and 121-A are primarily intermediate. Sample 119a-D exhibits intermediate compositions throughout its multi-spot analysis tests and felsic compositions in its single-spot analysis tests. The non-flow banded dikes (27b and 34) had the lowest silica contents out of all of the samples.

Figure 3.25 and 3.26 show multi-spot and single-spot analysis results plotted on an alkali vs. silica diagram. Exact rock types could not be specified due to the absence of Na_2O weight percent data, but weight percentages of SiO_2 and K_2O were used to plot lines on the diagrams to show the range of possible rock types for each sample. Each line is color coded according to their corresponding sample number. The red, blue and green dots plotted on the diagrams show sample chemistries of other samples sourced from felsic dikes located within the greater Mt. Jasper region measured in previous works. The red dots represent 37 Mt. Jasper sample

chemistries from the Mt. Jasper lithic source from Boisvert and Pollock (2009), the blue dots show 8 Mt. Jefferson-sourced artifacts and rhyolite samples from Baker (2016), and the green dot represents 1 Mt. Jasper rhyolite sample from Billings and Fowler-Billings (1975).

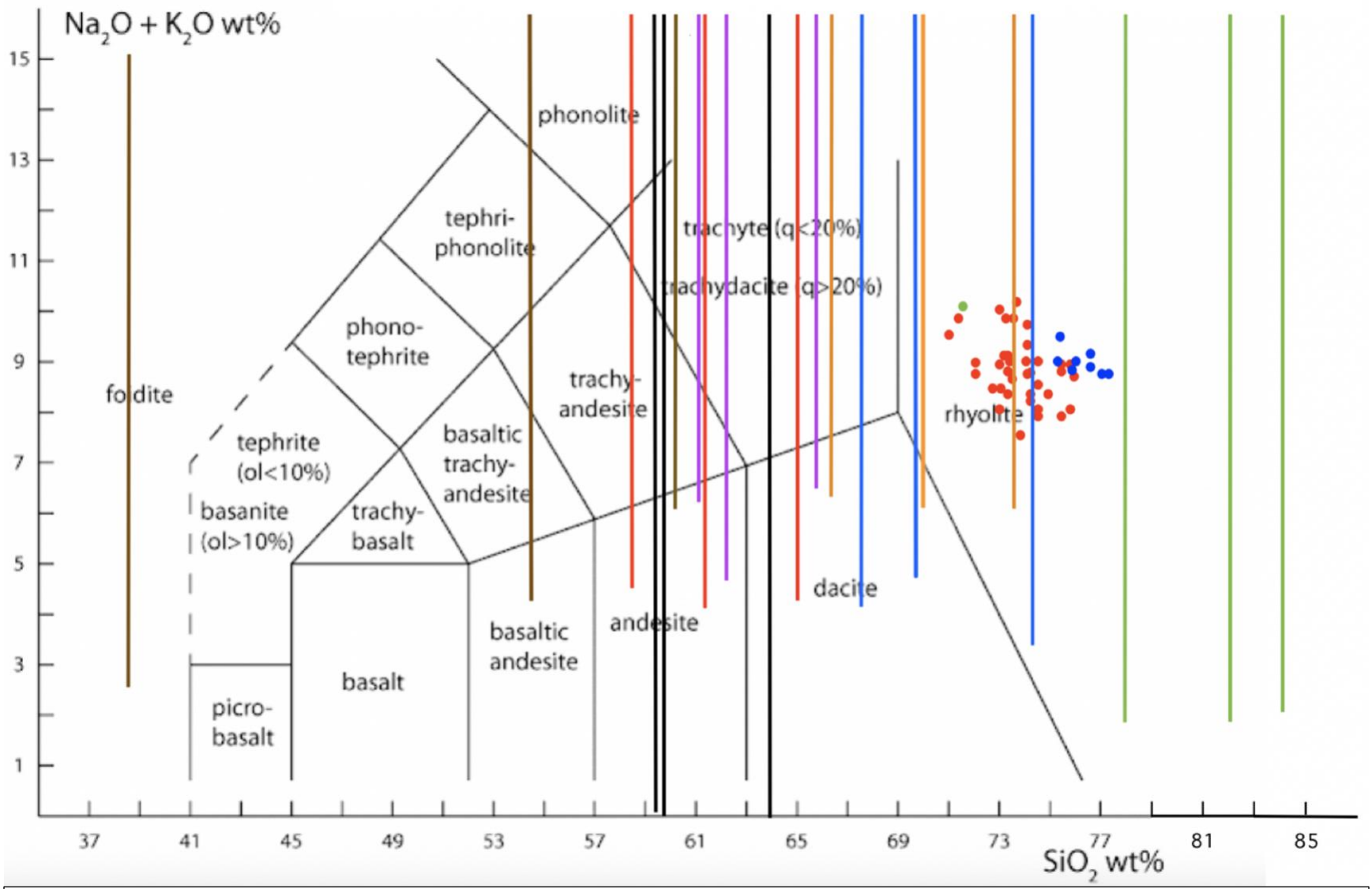

Figure 3.25: Multi-spot chemical analysis results plotted in lines on an alkali vs. silica diagram. Includes samples 119a-A (green), 119a-B (blue), 119a-D (black), 123 (orange), 34 (red), 121 (purple), and 27b (brown). Dots plotted on the diagram represent 37 Mt. Jasper rhyolite samples from Boisvert and Pollock (2009) (red), 8 Mt. Jefferson rhyolites from Baker (2016) (blue), and 1 Mt. Jasper rhyolite from Billings and Fowler-Billings (1975) (green).

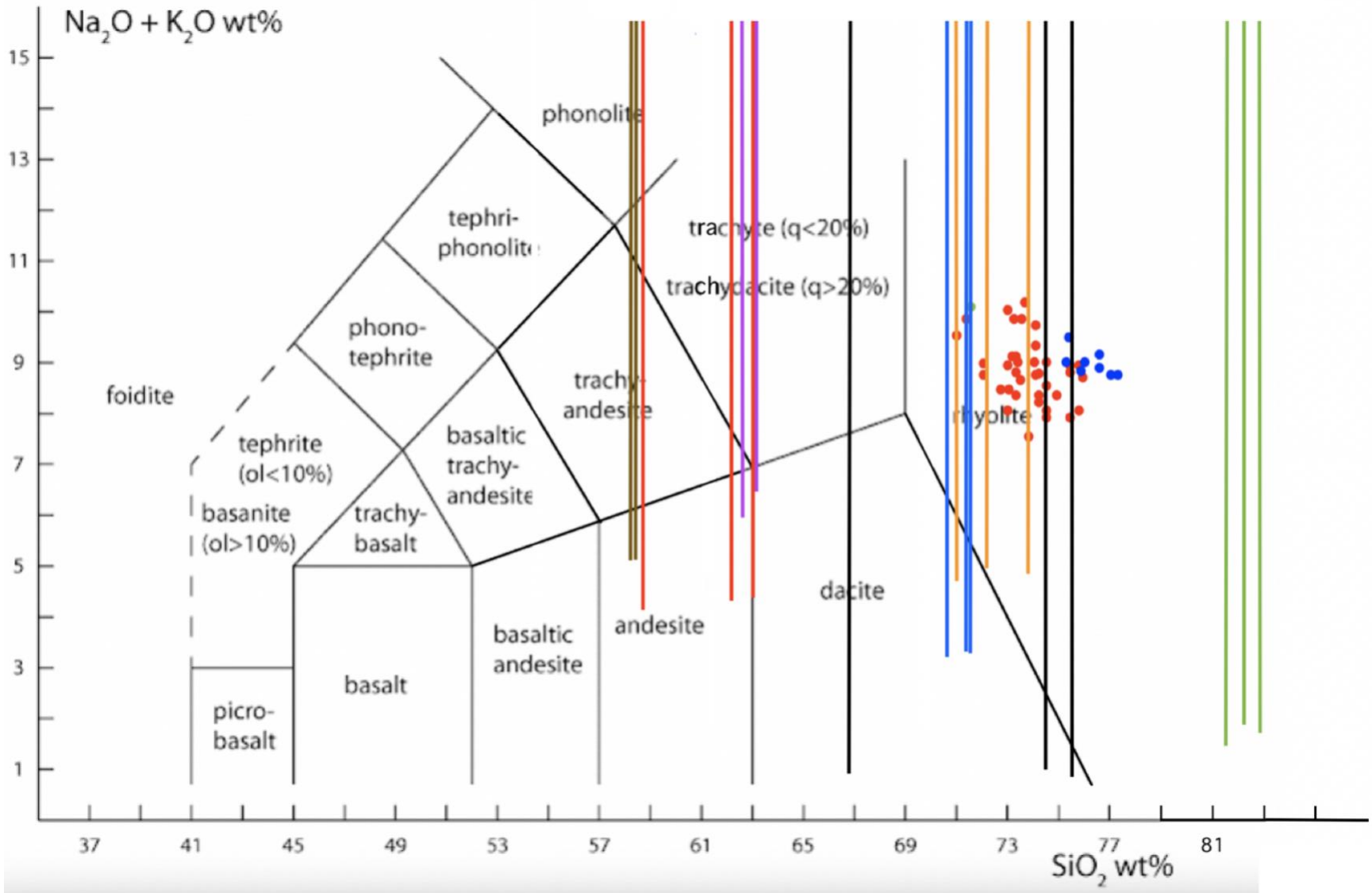

Figure 3.26: Single-spot chemical analysis results plotted in lines on an alkali vs. silica diagram. Includes samples 119a-A (green), 119a-B (blue), 119a-D (black), 123 (orange), 34 (red), 121 (purple), and 27b (brown). Dots plotted on the diagram represent 37 Mt. Jasper rhyolite samples from Boisvert and Pollock (2009) (red), 8 Mt. Jefferson rhyolites from Baker (2016) (blue), and 1 Mt. Jasper rhyolite from Billings and Fowler-Billings (1975) (green). Note that test 1 results for samples 27b and 121-A were omitted from this diagram due to faulty measurement collection.

According to these results, dikes 119a and 123 are the only ones that are likely to be accurately classified as rhyolite dikes. The majority of pXRF results for the remaining samples indicate mostly to entirely non-rhyolitic compositions. On the other hand, the 46 Mt. Jasper and Mt. Jefferson samples plotted from previous works are all indicative of strictly rhyolitic compositions. Furthermore, the sets of three similarly colored lines, which represent the three iterations of tests completed for each of the individual samples, are much more widely distributed in the multi-spot analysis than those plotted for the single-spot analysis. This suggests that the three areas tested for each sample in the multi-spot analysis bared varying chemical compositions.

Chapter 4: Discussion

4.1: Mechanisms of Flow Banding Formation

Although an absolute answer may not be reached, interpretation of the physical structures observed in the samples do allow inferences to be drawn about several possible mechanisms of flow banding formation in these dikes. Flow banding segmentation and production of other shear-related deformational structures, such as those imaged in figures 3.1 and 3.9 of the results, indicate that a shear component must have been present in whatever magmatic mechanism was responsible for the formation of the flow banding in these samples. These structures, as well as several other non-shear related structures, suggest that the flow banding present in these samples may be linked to one or more potential mechanisms of flow banding formation. Each of these possible mechanisms will be further discussed in the following subsections. These mechanisms are not distinguishable from one another given the results presented in this study alone, however, visual and/or chemical distinctions between them may be uncovered with further work.

4.1.1: Shear-Induced Fragmentation and Reannealing

The first possible mechanism of flow banding formation in these samples is shear-induced fragmentation and reannealing. The production of flow banding structures by magma fragmentation and reannealing is initiated by the generation of a differential velocity profile in the rates at which magmas flow within the volcanic conduit. As magma rises in the conduit, the melt that is directly adjacent to the conduit walls is subject to a frictional, dragging force. This force slows the rate of flow along the conduit walls, while the faster flowing magma at the center draws adjacent melt upwards as it continues to rise in the conduit (Gonnermann and Manga, 2003). This differential velocity profile is illustrated by the diagram in figure 4.1 from

Gonnermann and Manga (2003). Microscopic crystals nucleate in the slower moving magma at the conduit walls while shear stress, resulting from the downward-pulling frictional force against the conduit walls and upward-pulling force of the rising adjacent magma, inflicted in the conduit's margins causes the magma to break up into pieces (Gonnermann and Manga, 2003). The fragmented magma is then reincorporated back into the faster flowing core of the conduit, where it is then deformed and stretched by the movement of the surrounding magma as it continues to flow (Gonnermann and Manga, 2003). The crystal nucleation that occurs at the conduit walls locally alters the color of the magma, so the entrainment of the crystal-rich fragments within the crystal-poor surrounding melt and subsequent elongation of the fragments produces flow bands composed of highly concentrated crystals bordered by zones of crystal-poor melt (Gonnermann and Manga, 2003). The progressive stages of magma fragmentation, elongation and flow banding formation are depicted in figure 4.2, taken from Gonnermann and Manga (2003).

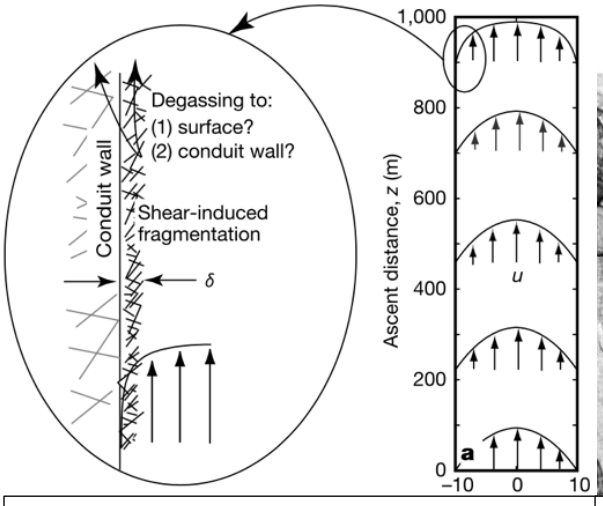

Figure 4.1: Differential velocity profile and subsequent shearing of magma within a volcanic conduit (Gonnermann and Manga, 2003).

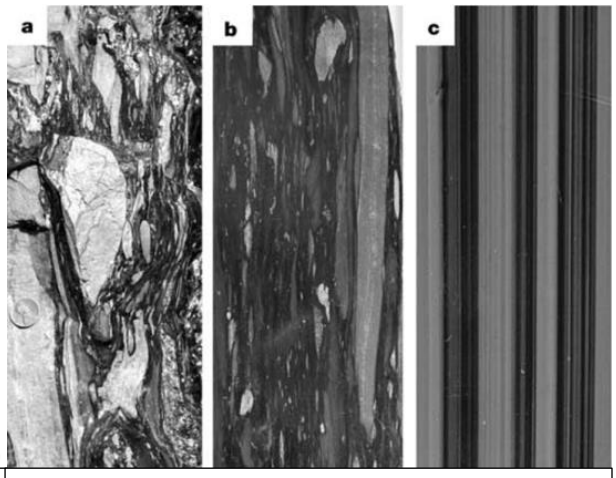

Figure 4.2: Progression of magma fragmentation (a), fragment elongation (b), and flow band formation (c) involved in the fragmentation and reannealing mechanism (Gonnermann and Manga, 2003).

4.1.2: Shear-Induced Production of Fracture Networks and Oxide Microlite Nucleation

Flow banding structures formed by shear-induced production of fracture networks and subsequent oxide microlite nucleation are similar to those that are produced by magma fragmentation and reannealing in that the processes of their formation both involve shear-induced brittle deformation of magma at the conduit margins in addition to ductile deformation via continued flow in the conduit. Like the fragmentation and reannealing mechanism, the fracturing and oxide microlite nucleation process begins with the infliction of shear stress on magma at the conduit walls that occurs with the production of a differential velocity profile within the melt as it rises in the conduit (Castro et al., 2005). In this instance, the added shear stress causes the magma to fracture in the margins of the conduit. The opening of these fractures results in a local depressurization within the area of each fracture (Castro et al., 2005). With this depressurization and the presence of water-rich vapor which saturates the fractured space, any magma immediately surrounding the perimeters of these fractures will experience rapid degassing and copious microlite nucleation around the borders of the fractures (Castro et al., 2005). This fracturing and microlite nucleation process is illustrated in figure 4.3, taken from Castro et al. (2005). These fractures then close to form areas of locally enriched oxide microlites, which are then redistributed throughout the melt and elongated into bands with continued flow in the conduit (Castro et al., 2005).

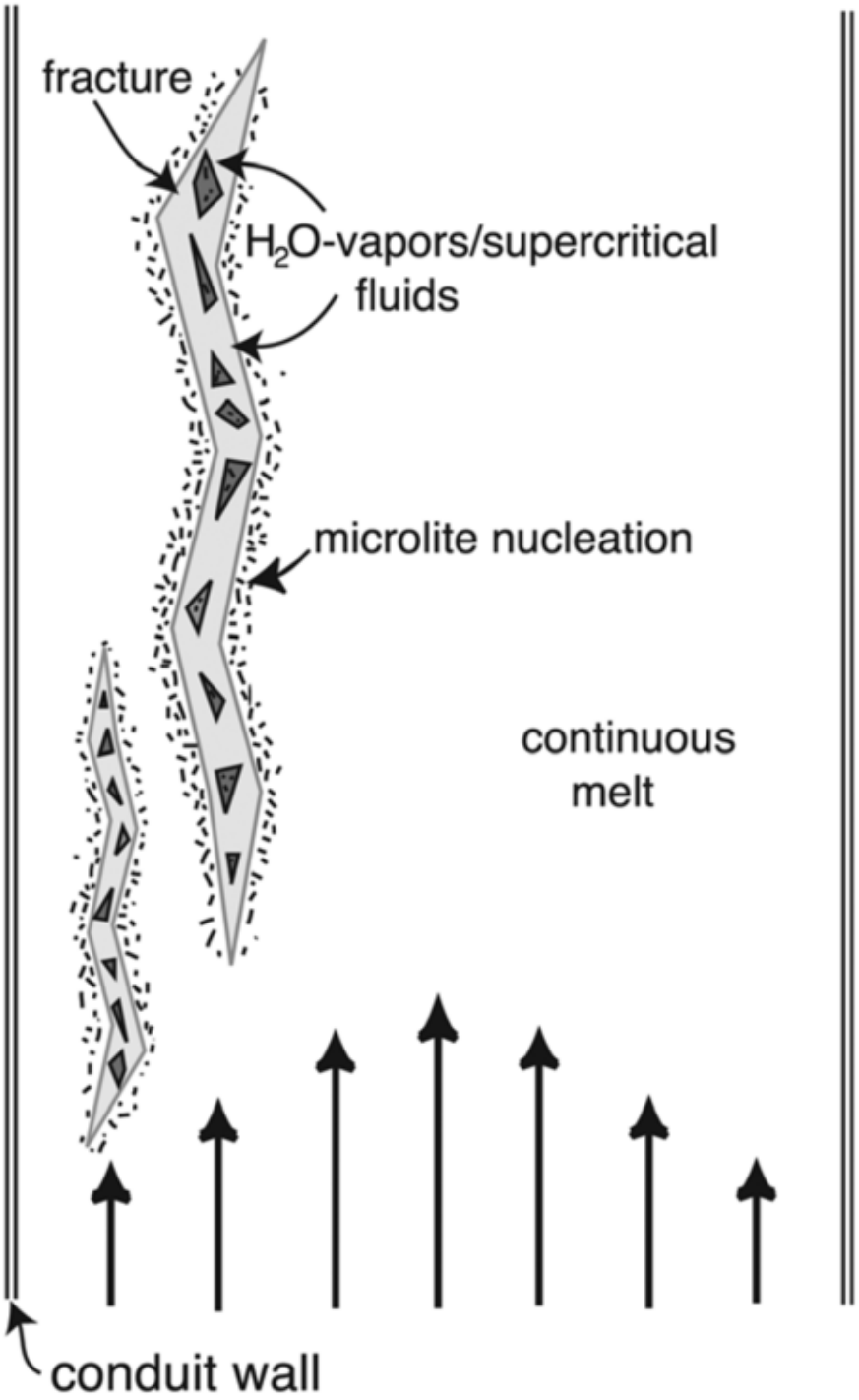

Figure 4.3: Shear-induced fracturing, degassing and microlite nucleation (Castro et al., 2005).

The flow banding structures produced by fragmentation and reannealing of magma and fracturing, degassing and oxide microlite nucleation are similar in that they are both comprised of regions of microlite-rich melt that have been produced by shear and elongated by laminar flow in the melt as it rises in the conduit. Ultimately, they both result in alternating bands of high and low microlite concentrations. The two mechanisms are distinguishable from each other, as the second mechanism which involves fracturing and degassing produces specifically oxide microlites, while the microlites produced during fragmentation and reannealing may be any number of non-oxide minerals present in these rocks. One might also expect that microlite composition and content could vary based on magma composition and pressure and temperature conditions in the conduit. In order to determine whether or not these mechanisms were responsible for the formation of the flow banding structures present in the samples focused on in this study, thin sections would need to be made from the samples. The presence or absence of microlite-rich bands visible in the thin sections would respectively prove or disprove these mechanisms' role in the formation of flow banding in in the Mt. Jasper dikes.

4.1.3: Mingling of Compositionally Distinct Magmas

The third possible mechanism that could have led to the formation of flow banding in these dikes is the mingling of compositionally distinct magmas. In this instance, two magmas of differing compositions would have been joined together in one magma chamber or conduit where they were then stretched and deformed together as the melt rose in the conduit (Seaman et al., 1995). This mingling and deformation would then produce a pattern of compositionally distinct alternating light and dark flow bands (Seaman et al., 1995). Although this mechanism of flow banding formation is not a direct result of shear stress in the conduit, the shear structures

observed in the samples may have been a result of shear stress exerted on the magmas as they flowed past each other during magma ascent and deformation (Seaman et al., 1995). Mingled magmas also have a tendency to begin to homogenize in some areas as they are continuously stretched and deformed, mixing the two magmas together as they rise in the conduit (Seaman et al., 1995). These initial stages of homogenization may explain the variability in band color and morphology found in dike 121. Figures 4.4 and 4.5 show two unweathered samples collected from dike 121. Sample 121-A exhibits very well pronounced, dark flow banding, while sample 121-C shows much lighter colored, poorly pronounced banding. This variability may be a result of homogenization of two compositionally distinct magmas where the two separate melts remained compositionally distinct in sample 121-A and became more homogenized in sample 121-C. In further work, this theory might be tested by sawing each sample in two along a boundary between a light and dark flow band. Bulk compositions could then be determined for each band type using pXRF tests. If their bulk compositions were characteristic of two separate rock types, it would suggest that the flow banding resulted from the mingling of two compositionally distinct magmas.

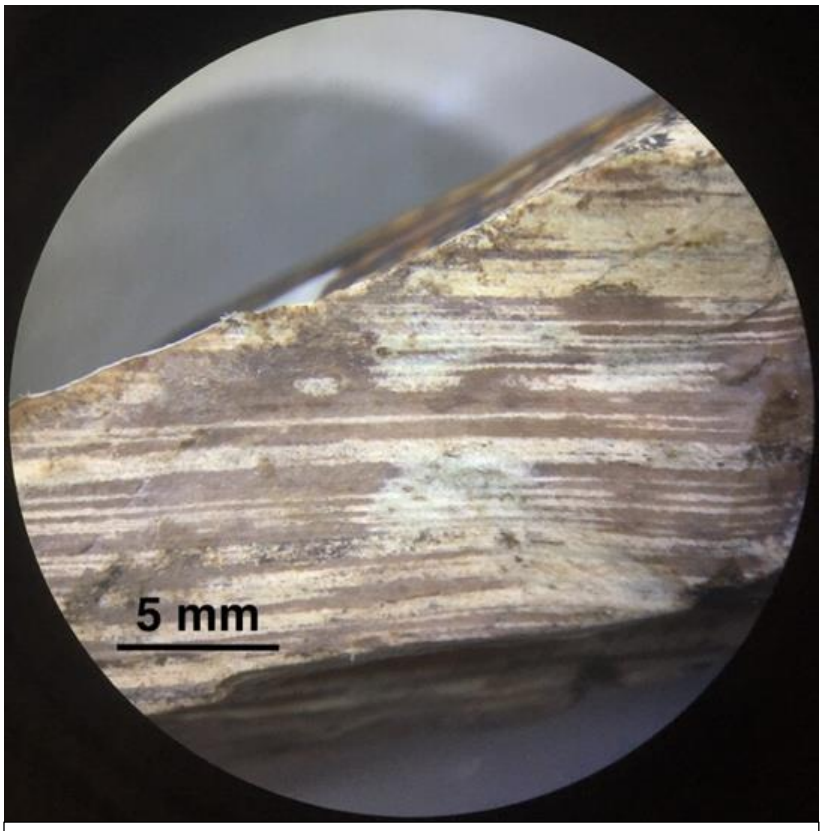

Figure 4.4: Unweathered, dark, very well pronounced flow banding in sample 121-A

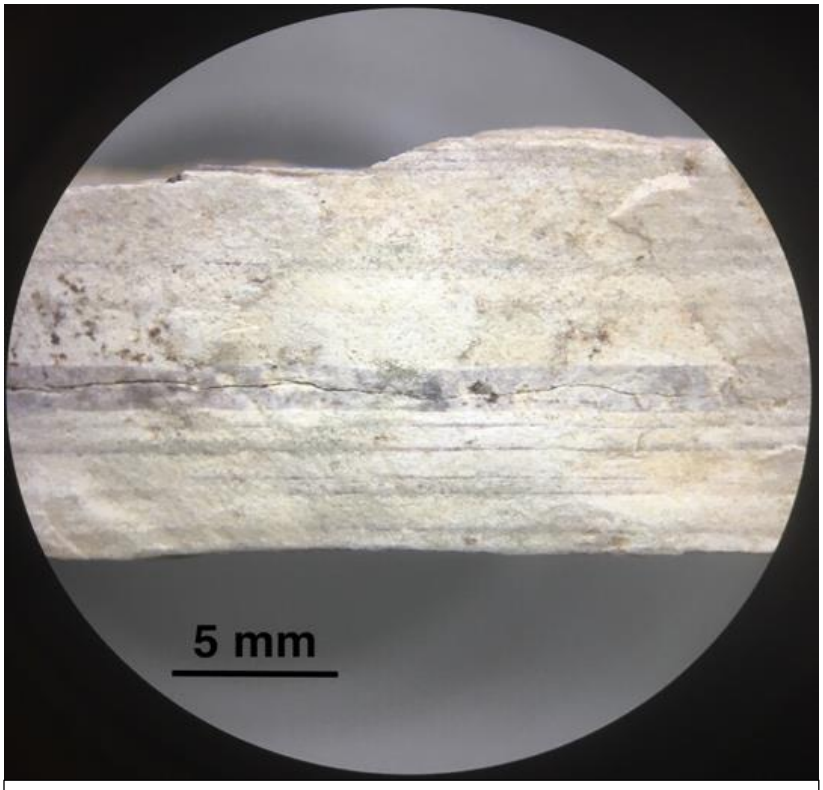

Figure 4.5: Unweathered, light, poorly pronounced flow banding in sample 121-C

4.1.4: Flow-Induced Stretching of Water Concentrated Zones in Magma

The final possible mechanism that may be responsible for the formation of flow banding in the Mt. Jasper felsic dikes is flow-induced stretching of magma containing zones of varying water concentrations. With this mechanism, regions of melt which contain high concentrations of H_2O are produced in the magma chamber or conduit, resulting in the zonation of contrasting H_2O-rich and H_2O-poor zones within the melt (Seaman et al., 2009). These water-rich zones may originate in a number of ways, such as through magma fragmentation and subsequent degassing with flow in the conduit, which would lower the volatile content in those areas of the melt, or with the presence of pre-existing vesicles containing high concentrations of water (Seaman et al., 2009). As the magma rises is the conduit, these volatile-rich zones are stretched and elongated with the flow of the melt, creating alternating bands that retain contrasting water concentrations (Seaman et al., 2009).

These differing zones of water concentration are also linked to the growth of spherulites, as spherulitic growth is favored by higher water concentrations due to the accelerated diffusion of cations that occur with the presence of water in the melt (Seaman et al., 2009). Previous work presented in the Seaman et al. (2009) study suggests that lighter colored flow bands retain higher water concentrations than darker colored bands, thus inhibiting the growth of larger spherulites in light bands (Seaman et al., 2009). However, the samples focused on in this study exhibit spherules that are exclusively confined to the darker flow bands. This pattern indicates that the flow banding must have formed prior to the growth of the spherulites and that the spherulitic growth favored the dark colored bands. Although this favoring contradicts the Seaman et al. (2009) findings, the confinement of spherules to the dark bands may still be somehow linked to water distribution in the melt. Additionally, the white rims surrounding the dark spherules could

possibly be a result of water rejection that may have occurred with the growth of the spherulites. In this case, water would have been pushed away from the spherules as they grew, subsequently quenching the surrounding melt to produce lighter colored rims (Seaman et al., 2009).

With particular consideration of the inconsistencies between the conclusions of the Seaman et al. (2009) study and the preferred growth of spherules within dark bands observed in samples examined in this study, further work is needed to determine the role of contrasting water concentrations in the development of flow banding and spherulite growth in these samples. One method of identification might lie in the examination of thin sections made from these samples. Flow bands produced by the zonation of contrasting water concentrations are defined by the juxtaposition of distinct colors of glass phases between the different bands (Seaman et al., 2009). In this case, the flow bands would not exhibit high microlite concentrations like they might with some of the other mechanisms of flow banding formation (Seaman et al., 2009). Another possible method for determining whether or not the flow bands were produced this way would be to chemically measure the water concentrations of each band type to determine if there is a significant difference in water concentration between the two.

4.2: Geochemistry

Compositional differences between the strictly rhyolitic Mt. Jasper and Mt. Jefferson samples from previous works and the more distributed sample compositions measured in this study are likely a result of compositional variation between the areas from which the samples were sourced. Samples from the previous works were all collected from archaeological lithic sources, where most of the samples in this study were not. Dike 119a samples were collected at a Mt. Jasper archaeological site, which explains why the 119a samples were more consistent with

the rhyolitic sample compositions from previous works. Sample 123, sourced from the previously undiscovered dike, also exhibited rhyolitic compositions similar to those from previous works. This observation may be of value to archaeologists, as this newly discovered dike shares similar properties with the archaeological site dikes, meaning that rhyolite from dike 123 would have been similarly useful for crafting tools and projectiles. With further investigation, this dike could potentially uncover a new, undiscovered historical mining site.

A comparison of the dramatic compositional variation found between the multi-spot chemical analysis measurements and the narrowly distributed single-spot analysis measurements confirms that there is in fact compositional variation within each of the individual samples. These compositional differences likely arose from one of two sources of variation. The first possible source lies within the weathering of the sample. Although the pXRF measurements were collected from the least weathered areas of the sample, it is possible that slight differences in weathering across the samples' surfaces may have altered the chemistries between the different analyzed areas. The second, more likely possibility is that there may have been different ratios phenocrysts to groundmass or of dark to light bands within the measurement window between each of the multi-spot analysis tests. If this is the source of the variation, it would mean that the dark and light flow bands are compositionally distinct, which would be consistent with the four previously proposed possibilities for flow banding formation, as each of those mechanisms would produce compositionally distinct flow banding.

Chapter 5: Conclusions

Flow banding structures in the Mt. Jasper felsic and intermediate composition dikes are most likely a result of either one or a combination of multiple of the following mechanisms of flow banding production: 1) shear-induced fragmentation and reannealing of magma in the volcanic conduit, 2) shear-induced production of fracture networks and subsequent oxide microlite nucleation, 3) mingling of two compositionally distinct magmas, or 4) flow-induced stretching of magma containing zones of varying water concentrations. The results presented in this study alone are not sufficient for determining which of these specific mechanisms are responsible for the flow banding in these dikes or how these processes may have played a role in their formation, however further work may narrow down these distinctions. This further work might involve the determination of the microstructural/textural features and compositions which distinguish the darker flow bands from the lighter surrounding rock (i.e. differences in microlite concentration, glass phase, rock types, water content). Determination of these band distinctions would require thin section examination as well as separate chemical analyses for both the darker flow bands and the bordering light-colored band varieties.

References:

Baker, S., 2016, Bedrock Geology of the Southern Half of the Jefferson 7.5' Quadrangle, New Hampshire [Bachelor of Science: Bates College, p. 1-74 p.

Bell, D.J., Nadrljanski, M.M., n.d., X-ray tube: Radiology Reference Article: X-Ray Tube, https://radiopaedia.org/articles/x-ray-tube-1?lang=us (accessed December 2020).

Billings, M. P., and Fowler-Billings, K., 1975, Geology of the Gorham Quadrangle: New Hampshire-Maine, State of New Hampshire, Department of Resources and Economic Development, v. 6.

Boisvert, R., and Pollock, S. G., 2009, The Archaeology and Geology of the Mount Jasper Lithic Source: The New Hampshire Archaeologist, v. 49, p. 37-48.

Boisvert, R., 1992, The Mount Jasper lithic source, Berlin, New Hampshire: National register of historic places nomination and commentary: Archaeology of Eastern North America, p. 151-165.

Castro, J. M., Dingwell, D. B., Nichols, A. R., and Gardner, J. E., 2005, New insights on the origin of flow bands in obsidian: Special Papers - Geological Society of America, v. 396, p. 55.

Faure, S., Tremblay, A., Malo, M., and Angelier, J., 2006, Paleostress analysis of Atlantic crustal extension in the Quebec Appalachians: The Journal of Geology, v. 114, no. 4, p. 435-448.

Gonnermann, H., and Manga, M., 2003, Explosive volcanism may not be an inevitable consequence of magma fragmentation: Nature, v. 426, no. 6965, p. 432-435.

Gonnermann, H., and Manga, M., 2004, Flow banding in volcanic rocks: A record of multiplicative magma deformation: AGUFM, v. 2004, p. V41A-1364.

Gottsmann, J., and Dingwell, D., 2001, Cooling dynamics of spatter-fed phonolite obsidian flows on Tenerife, Canary Islands: Journal of Volcanology and Geothermal Research, v. 105, no. 4, p. 323-342.

Gramly, R. M., and Cox, S. L., 1976, A Prehistoric Quarry-Workshop at Mt. Jasper, Berlin, New Hampshire: Man in the Northeast, v. 11, p. 71-74.

Guthrie, J.M., 1996, Overview of XRF (J. R. Ferguson, Ed.): The Archaeometry Laboratory at the University of Missouri Research Reactor, https://archaeometry.missouri.edu/xrf_overview.html (accessed October 2020).

Hausback, B. P., 1987, An extensive, hot, vapor-charged rhyodacite flow, Baja California, Mexico: The Emplacement of Silicic Domes and Lava Flows, Geol. Soc. Am. Spec. Pap, v. 212, p. 111-118.

McHone, J. G., Ross, M. E., and Greenough, J. D., 1987, Mesozoic dyke swarms of eastern North America: Mafic dyke swarms. Edited by HC Halls and WF Fahrig. Geological Association of Canada, Special Paper, v. 34, p. 279-288.

Munro, M., 1990, Banding in igneous rocks, Petrology: Boston, MA, Springer US, p. 48-51.

Olympus, 2020, Vanta Family X-Ray Fluorescence Analyzer: User's Manual DMTA-10072 01EN, Rev. F: https://www.scribd.com/document/475957537/VANTA-PMI-Operating-Manual-pdf

Pollock, S. G., Hamilton, N. D., and Boisvert, R. A., 2008, Archaeological geology of two flow-banded spherulitic rhyolites in New England, USA: their history, exploitation and criteria for recognition: Journal of Archaeological Science, v. 35, no. 3, p. 688-703.

Rust, A., Cashman, K., and Wallace, P., 2004, Magma degassing buffered by vapor flow through brecciated conduit margins: Geology, v. 32, no. 4, p. 349-352.

Smith, J. V., 1996, Ductile-brittle transition structures in the basal shear zone of a rhyolite lava flow, eastern Australia: Journal of Volcanology and Geothermal Research, v. 72, no. 3-4, p. 217-223.

Seaman, S. J., Dyar, M. D., and Marinkovic, N., 2009, The effects of heterogeneity in magma water concentration on the development of flow banding and spherulites in rhyolitic lava: Journal of Volcanology and Geothermal Research, v. 183, no. 3-4, p. 157-169.

Seaman, S. J., Scherer, E. E., and Standish, J. J., 1995, Multistage magma mingling and the origin of flow banding in the Aliso lava dome, Tumacacori Mountains, southern Arizona: Journal of Geophysical Research: Solid Earth, v. 100, no. B5, p. 8381-8398.